International Journal of Geosciences, 2025, 16(7), 464-504
https://www.scirp.org/journal/ijg
ISSN Online: 2156-8367
ISSN Print: 2156-8359

Fusion of Terrestrial Laser Scanning and UAV Photogrammetry for Advanced Landslide Monitoring: Integrated Assessment of the Kshetrapal Landslide, Chamoli District, Uttarakhand, India

Ashok Anand

Geomatics Engineering Group, Department of Civil Engineering, Indian Institute of Technology Roorkee, Uttarakhand, India
Email: a_anand@ce.iitr.ac.in

How to cite this paper: Anand, A. (2025) Fusion of Terrestrial Laser Scanning and UAV Photogrammetry for Advanced Landslide Monitoring: Integrated Assessment of the Kshetrapal Landslide, Chamoli District, Uttarakhand, India. *International Journal of Geosciences*, **16**, 464-504.
https://doi.org/10.4236/ijg.2025.167023

Received: February 17, 2025
Accepted: July 28, 2025
Published: July 31, 2025

Abstract

This study presents an integrated TLS-UAV photogrammetry approach for monitoring the Kshetrapal landslide in Chamoli, Uttarakhand, India, where steep slopes (45˚ - 65˚) and dense vegetation challenge conventional methods. By combining terrestrial laser scanning (TLS) and unmanned aerial vehicle (UAV) photogrammetry, the method enhances ground control point (GCP) density in visible areas while employing assumed control points (ACPs) derived from TLS data to reconstruct UAV models in obscured zones. The Newton integration model quantifies discrepancies between coordinate displacement (CD) and real displacement (RD), achieving sub-pixel accuracy (errors: 0.0235 - 0.8021 pixels) validated through field data. Key results include a 40% improvement in spatial coverage through TLS-UAV fusion, reduced RMSE to 0.2 m in fused point clouds, and detection of monsoon-induced displacements up to 1.7 m during the 2023 reactivation. The approach demonstrates 26% higher accuracy than traditional GCP-dependent methods in Himalayan conditions, offering a replicable framework for landslide risk management in geologically sensitive regions. Validated through multi-temporal datasets and real-world scenarios, this methodology addresses critical gaps in accessibility and precision, providing actionable insights for disaster management agencies like the Uttarakhand State Disaster Management Authority.

Keywords

Data Fusion, Landslide Monitoring, Terrestrial Laser Scanning (TLS), Unmanned Aerial Vehicle (UAV), Kshetrapal Landslide

1. Introduction

Landslides are among the most destructive natural hazards affecting mountainous regions worldwide, causing extensive damage to infrastructure, loss of life, and significant socio-economic disruption. The Himalayan belt, stretching across northern India, Nepal, and Bhutan, is one of the most landslide-prone areas on the planet due to its complex geological structures, steep slopes, high rates of precipitation, and frequent seismic activity [1] [2]. Within this region, the Indian state of Uttarakhand is particularly vulnerable, with numerous documented landslides occurring annually, especially during the monsoon season. The Kshetrapal landslide, located in Chamoli district, Uttarakhand, exemplifies the challenges faced in monitoring and managing landslide hazards in such rugged and dynamic environments.

1.1. The Challenge of Landslide Monitoring in the Himalayas

Monitoring landslides in the Himalayas is a formidable task due to several interrelated factors. First, the region's topography is characterized by steep slopes (often exceeding 45˚), deep valleys, and rapidly changing elevations, which complicate both field access and the deployment of traditional monitoring equipment [3]. Second, dense vegetation cover, especially in the lower and middle Himalayan ranges, obscures the ground surface, making it difficult to obtain accurate measurements of terrain changes using optical remote sensing or ground-based surveys. Third, the high frequency of extreme weather events, such as intense rainfall during the monsoon and occasional cloudbursts, triggers rapid slope failures and exacerbates ground instability [4] [5].

Conventional landslide monitoring approaches, such as the use of total stations, GNSS (Global Navigation Satellite System) receivers, inclinometers, and extensometers, are effective for measuring displacement at specific points but are limited in spatial coverage and often require direct access to hazardous or inaccessible locations [6]. Moreover, these methods can be labour-intensive, time-consuming, and potentially dangerous for field personnel, particularly in the aftermath of major slope failures or during inclement weather.

1.2. Advances in Remote Sensing for Landslide Monitoring

In recent years, advances in remote sensing technologies have revolutionized the field of landslide monitoring, offering new possibilities for rapid, accurate, and non-contact data acquisition over large and difficult-to-access areas [7]. Among these technologies, Unmanned Aerial Vehicles (UAVs) and Terrestrial Laser Scanning (TLS) have emerged as particularly valuable tools.

1.3. Unmanned Aerial Vehicles (UAVs)

UAVs, commonly known as drones, have gained widespread popularity for environmental monitoring due to their flexibility, cost-effectiveness, and ability to capture high-resolution imagery and topographic data [5]. Equipped with ad-

vanced cameras and sensors, UAVs can generate detailed Digital Elevation Models (DEMs) and orthophotos, enabling the detection and quantification of surface changes associated with landslide activity. UAV-based photogrammetry is especially useful in mountainous regions, where ground access is limited and rapid data collection is essential for timely hazard assessment [8].

However, UAV surveys are not without limitations. The accuracy of UAV-derived models depends heavily on the availability and precise placement of Ground Control Points (GCPs), which are often difficult to establish in densely vegetated or unstable terrain [9] [10]. Furthermore, UAV flights can be affected by adverse weather conditions, battery limitations, and regulatory restrictions, all of which can constrain the frequency and extent of data acquisition.

1.4. Terrestrial Laser Scanning (TLS)

TLS, also known as ground-based LiDAR, provides highly accurate three-dimensional point clouds of the terrain by emitting laser pulses and measuring their return times. TLS is capable of capturing fine-scale surface features and subtle deformations, making it ideal for monitoring landslides and other geomorphological processes [11]. Unlike UAVs, TLS does not rely on external lighting conditions and can operate effectively under dense canopy cover, provided there is a clear line of sight between the scanner and the target surface. Nevertheless, TLS also has its drawbacks. The technology is typically limited by its range and field of view, resulting in blind spots behind obstacles such as boulders, trees, or steep terrain. Multiple scan positions are often required to achieve comprehensive coverage, which can increase survey time and complexity. Additionally, the integration of TLS data with other spatial datasets (such as UAV-derived models) requires careful alignment and calibration to ensure geometric consistency [10].

1.5. The Rationale for Data Fusion

Given the complementary strengths and weaknesses of UAV and TLS technologies, there is growing interest in integrating data from both sources to enhance landslide monitoring capabilities [9]-[11]. Data fusion approaches combine the high spatial resolution and flexibility of UAV photogrammetry with the geometric accuracy and detailed surface representation of TLS, resulting in more complete and reliable models of landslide-affected terrain.

Recent studies have demonstrated the benefits of such integration. For example, [10] showed that fusing UAV and TLS point clouds improved the assessment of forest structure by filling gaps in coverage and reducing positional errors. Similarly, [9] reported that combining low-cost UAV and TLS data provided a more complete 3D visualization of buildings and terrain features, particularly in areas where GCP placement was challenging. [11] applied TLS-UAV fusion for post-earthquake 3D modeling of cultural heritage sites, highlighting the method's potential for rapid damage assessment in complex environments.

In the context of landslide monitoring, data fusion not only enhances spatial

coverage but also improves the accuracy of displacement measurements, which is critical for early warning and risk mitigation (Albanwan *et al.*, 2024; Zhu *et al.*, 2024) [6] [12]. By leveraging TLS-derived control points and integrating them with UAV photogrammetry, it is possible to reduce reliance on traditional GCPs and achieve robust model calibration even in inaccessible or vegetated areas (Chauhan *et al.*, 2021; Panagiotidis *et al.*, 2022) [9] [10].

1.6. The Kshetrapal Landslide: A Case Study

The Kshetrapal landslide, located in the Chamoli district of Uttarakhand, is a representative example of the challenges and opportunities associated with landslide monitoring in the Himalayas. The site is characterized by steep slopes (ranging from 45˚ to 65˚), significant elevation differences (400 - 800 meters), and a history of recurrent slope failures, particularly during the monsoon season. The landslide poses a persistent threat to the Char Dham pilgrimage route, a vital transportation corridor for both local residents and religious tourists [1].

Traditional monitoring efforts at Kshetrapal have been hindered by difficult terrain, dense vegetation, and frequent slope movements, which limit the effectiveness of ground-based surveys and the deployment of permanent instrumentation. In this context, the integration of TLS and UAV photogrammetry offers a promising solution for overcoming these challenges and providing timely, accurate information on landslide dynamics.

1.7. Methodological Innovations

This study builds on recent advances in multi-sensor data fusion and geospatial analysis to develop a robust framework for landslide monitoring at Kshetrapal. The approach involves several key innovations:

1) Enhanced GCP/ACP Workflow: By using TLS to identify and establish a dense network of ground control points (GCPs) in accessible areas and deriving assumed control points (ACPs) in obscured or inaccessible zones, the method reduces dependence on traditional GCPs. This is particularly important in Himalayan terrain, where GCP deployment is often impractical or unsafe [9] [10].

2) Multi-Sensor Data Fusion: The integration of TLS point clouds (e.g., from a FARO S350 + scanner) and UAV-derived digital surface models (DSMs) (e.g., from a DJI Phantom 4 RTK) is achieved using advanced registration algorithms, such as the Iterative Closest Point (ICP) method [10] [11]. This fusion process fills coverage gaps, mitigates blind spots, and improves the geometric fidelity of the resulting 3D models.

3) Advanced Displacement Analysis: The application of the Newton integration model enables precise calculation of landslide displacement by quantifying the discrepancy between coordinate displacement (CD) and real displacement (RD). This allows for sub-pixel accuracy in displacement measurements, even in areas with limited direct observation [13].

4) Operational Validation: The methodology is validated using multi-tem-

poral datasets collected during the 2023 monsoon season, capturing the reactivation of the Kshetrapal landslide and enabling the detection of displacements up to 1.7 meters. The results are benchmarked against existing monitoring data and ground truth observations to assess accuracy and reliability.

1.8. Significance and Broader Impacts

The integrated TLS-UAV framework developed in this study addresses critical gaps in landslide monitoring in the Himalayas and offers several important benefits:

1) Improved Spatial Coverage: By combining TLS and UAV data, the method achieves comprehensive coverage of complex terrain, including areas that are inaccessible or obscured by vegetation.

2) Enhanced Accuracy: The fusion of high-resolution point clouds and the use of advanced calibration techniques result in lower RMSE values and more reliable displacement measurements.

3) Operational Efficiency: The approach reduces the need for extensive fieldwork and GCP deployment, enabling safer and more efficient data collection in hazardous environments.

4) Scalability and Replicability: The methodology can be adapted to other landslide-prone regions and integrated with emerging technologies such as real-time edge computing, machine learning, and IoT-based early warning systems [4] [14].

By providing a robust, flexible, and validated framework for landslide monitoring, this research contributes to improved hazard assessment, early warning, and risk mitigation in vulnerable mountain regions. The findings have direct implications for disaster management agencies, infrastructure planners, and local communities in Uttarakhand and beyond.

1.9. Structure of the Paper

The remainder of this paper is organized as follows. Section 2 provides a review of the literature on landslide monitoring using TLS and UAV techniques. In Section 3, the suggested technique is thoroughly described. Section 4 presents the findings and assessments of errors. Lastly, the paper concludes in Section 5.

2. Related Work

Recent literature on landslide monitoring highlights a growing emphasis on the integration of Terrestrial Laser Scanning (TLS) and Unmanned Aerial Vehicle (UAV) photogrammetry, particularly for challenging environments where steep slopes, dense vegetation, and limited accessibility hinder traditional approaches. [15] proposed a TLS-UAV fusion strategy specifically designed for high-altitude regions where sightlines are obstructed and reliable ground control points (GCPs) are difficult to establish. Their methodology incorporates real-time kinematics-based control points (RCPs), lower-precision TLS control points (TCPs), and as-

sumed control points to adapt to complex terrain and effectively analyze surface deformation. Their findings demonstrate that careful assessment of GCP precision, quantity, and the use of assumed tie points (ATPs) can significantly enhance model accuracy, even when some GCPs are of lower quality. The fusion approach achieved superior displacement measurement compared to using GCPs alone, and multi-source data from the Xinhua landslides in Baoxing County, China, confirmed the method's ability to deliver high-accuracy monitoring in otherwise inaccessible conditions. Similarly, [16] advanced the field by developing a simulation-based mapping approach that fuses UAV photogrammetry and TLS for difficult terrain. By incorporating TLS-derived control points into UAV models, their method overcomes the coverage and accuracy limitations of each technique when used independently. The fusion process, stabilized by the high-density point clouds from TLS, was validated with a 3D model variation comparison tool that measures terrain simulation distance and rotational alignment using the ICP algorithm. Applied to the Yebatan hydroelectric project in Southwest China, this strategy improved model accuracy by 26% and more than doubled the mapping range, demonstrating the value of UAV-TLS integration for hostile environments. [17] introduced a geometric transformer-based 3D point cloud monitoring method for steep railway slopes, which leverages deep learning to enhance UAV point cloud precision from 37.44 mm to 8.11 mm. Their approach reduces noise and improves coherence across scales through dynamic division and multi-scale blurring, while integrating UAV and TLS datasets to compensate for occlusions and missing data in TLS scans. The geometry converter algorithm further aligns the datasets, ultimately achieving a model accuracy of 5.11 mm. In the context of post-disturbance landscape monitoring, Alex, [18] demonstrated the effectiveness of combining aerial photography and terrestrial LiDAR (t-LiDAR) for tracking sedimentation and soil loss in a Greek coastal watershed following a wildfire. Their analysis showed that initial post-fire rainfall events generated significant silt deposition, which diminished as vegetation recovered, with UAV and TLS data capturing both micro-topographic changes and broader erosion trends. This approach provided valuable insights for erosion control and landscape management in wildfire-prone areas. [19] compared the accuracy of UAV photogrammetry and TLS for quarry monitoring, finding that both methods produce high-quality point clouds, though TLS offers superior point density and terrain detail for digital terrain model (DTM) generation. UAV photogrammetry, however, was noted for its speed, cost-effectiveness, and operational flexibility. In a related study, [20] integrated TLS, UAV photogrammetry with structure-from-motion and multi-view stereo (SfM-MVS), and aerial laser scanning (ALS) to monitor talus cone evolution and boulder deformation, demonstrating the robustness of combining multiple geodetic and remote sensing methods for alpine geohazard monitoring. [21] utilized multi-temporal UAV imagery and topographic data to investigate geomorphic changes in Pakistan's Nara and Nokot active landslides. By applying the Geomorphic Change Detection (GCD) tool and analyzing factors such as topo-

graphic wetness, slope, and displacement, they quantified significant erosional displacements and volumetric changes, demonstrating the utility of UAV-based monitoring for active landslide sites. [22] explored the integration of machine learning with surface displacement analysis, using a support vector machine and the augmented Small Baseline Subset (SBAS) approach to develop an integrated model that more accurately predicts surface deformation. Their approach combined multiple environmental and geomorphic factors to improve the reliability of landslide risk assessments. [23] focused on rapid slope characterization and deformation assessment, particularly for emergency inspections and landslide monitoring. They developed an automatic discontinuity recognition system using k-means fuzzy clustering to extract geometric information from point clouds, and a quantitative displacement evaluation method based on the M3C2 algorithm to track local deformation trends. These tools enable fast, accurate assessment of unstable slope blocks during crisis response.

[24] addressed the challenge of data continuity in landslide monitoring by integrating field surveys, UAV photogrammetry, and GNSS tracking at the Wulipo landslide in the Baihetan Reservoir area. Their approach used sub-pixel offset tracking (SPOT) to derive displacement vectors from UAV datasets and linked field data to reservoir water levels, providing a comprehensive understanding of buoyancy-driven landslide acceleration. Review Summary:

The literature consistently identifies key limitations of using TLS and UAV systems independently. TLS is prone to blind spots caused by terrain obstructions and dense vegetation, while UAV photogrammetry depends on well-distributed, high-accuracy GCPs, which are often unfeasible in inaccessible areas. Additionally, noise and low-quality datasets can hinder the effectiveness of TLS-UAV fusion methods, including those utilizing the ICP algorithm, especially in complex terrains where high-precision displacement measurements are crucial. Dynamic environmental factors such as steep slopes and rapidly changing geological conditions further complicate monitoring efforts. Existing approaches often lack adaptability for high-risk, rapidly changing environments, and while some studies have incorporated machine learning for monitoring, robust integration of multiple data sources remains a challenge. Multi-temporal UAV imagery and static detection devices yield valuable measurements but fall short in providing real-time analysis during emergencies. Another significant gap is the lack of seamless integration between drone surveys, GNSS tracking, and field data, which undermines data continuity and integrity. Environmental triggers like reservoir-induced landslides further highlight the need for adaptive, integrated monitoring solutions. To address these challenges, future research should focus on developing hybrid adaptive integration models that combine dynamic TLS and UAV data using advanced feature alignment and control point techniques responsive to real-time changes. Machine learning-driven integration can enhance data accuracy and resolve alignment issues, while predictive models based on the Newton method and reinforcement learning can reduce bias in blind spots. Resilient data integration systems,

partially combining UAV, GNSS, and field data, are needed to ensure continuous, actionable insights. Finally, real-time monitoring frameworks tailored to specific geological and hydrological contexts could transform landslide risk management in inaccessible and complex terrains.

3. Study Area and Data Acquisition

This study centres on the Kshetrapal landslide in Chamoli, Uttarakhand, India geologically sensitive zone within the Himalayan range. The area is marked by steep slopes, with elevation differences ranging from 500 to 900 meters and inclines between 45˚ and 65˚. Kshetrapal has a well-documented history of landslides, primarily triggered by heavy monsoonal rains and seismic activity. Data collection commenced immediately following a major landslide event in June 2023, which blocked the main access route to nearby settlements. To capture comprehensive terrain data and geodetic coordinates, a combination of Real-Time Kinematic (RTK) GPS, Terrestrial Laser Scanning (TLS) using a FARO S350+ (Figure 1 and Figure 2), and UAVs (SNAP-M) (Figure 3) was deployed.

Figure 1. FARO S359+ (Scanner).

Figure 2. Scanning by FARO S350+ of Kshetrapal landslide.

Figure 3. SNAP-M UAV.

UAV photogrammetry was initially used to map visible areas of the landslide. However, significant blind spots were encountered, limiting the effectiveness of monitoring and deformation analysis. Subsequent data collection campaigns were conducted after emergency road construction restored limited ground access. These challenges underscored the limitations of conventional monitoring technologies in complex terrains like Kshetrapal. Consequently, the study adopted an integrated approach, combining UAV photogrammetry, TLS data, and advanced analytical models to enhance accuracy and coverage in landslide monitoring.

3.1. Kshetrapal Landslide

The Kshetrapal landslide is located in Chamoli district, Uttarakhand, within the coordinates 29˚50′N to 30˚40′N and 78˚40′E to 79˚50′E (Figures 4-8). This region is highly susceptible to frequent landslide hazards. Chamoli, the second largest district in Uttarakhand, is strategically significant as it shares its northern boundary with Xizang (China) and borders several other districts including Uttarkashi, Rudra Prayag, Tehri Garhwal, Almora, Baleshwar, and Pithoragarh.

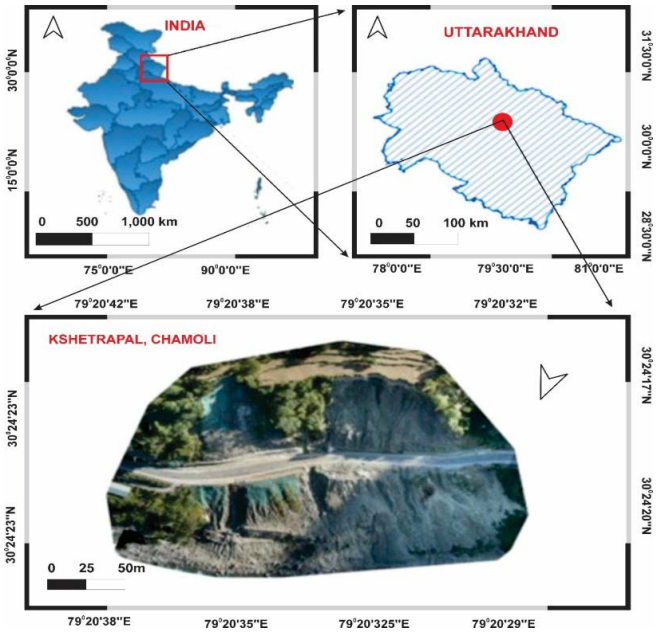

Figure 4. Kshetrapal landslide map in District Chamoli, Uttarakhand.

Figure 5. Shape file of landslide.

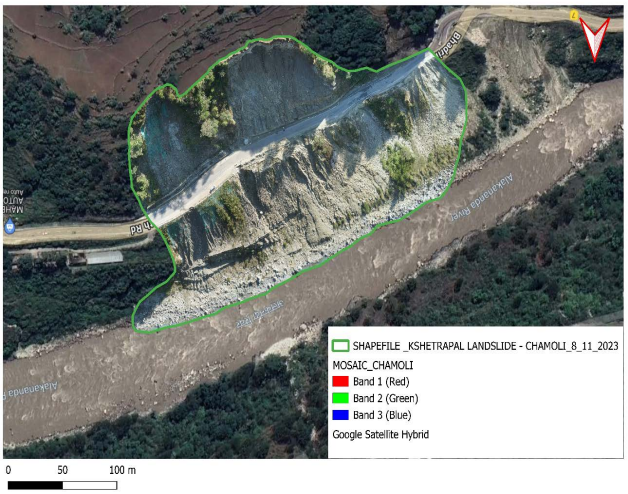

Figure 6. Mosaic landslide.

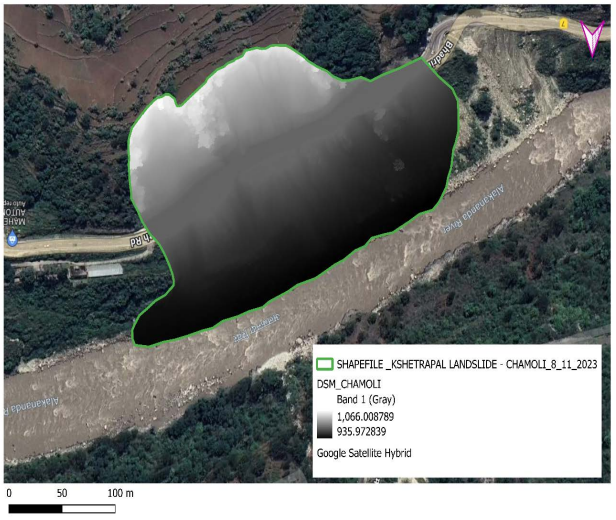

Figure 7. DSM of Kshetrapal landslide.

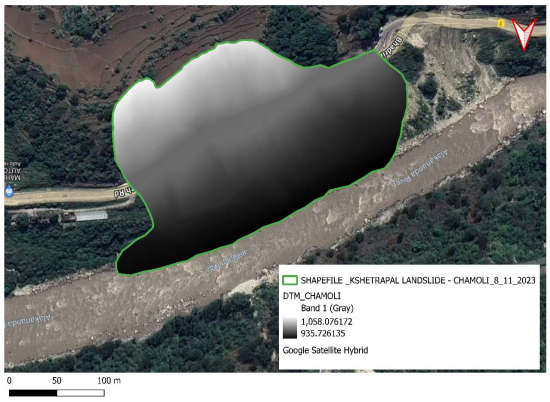

Figure 8. DTM of Kshetrapal landslide.

3.2. Research Contribution

In this research, the Kshetrapal landslide was assessed using UAVs equipped with high-resolution cameras, which enabled rapid mapping of the landslide's extent and identification of unstable slopes (**Figure 9**). TLS provided precise ground-level measurements, facilitating the creation of detailed 3D terrain models and the analysis of post-landslide surface changes. This comprehensive methodology improved the understanding of landslide mechanisms, supported risk assessment, and informed the development of emergency response strategies and sustainable mitigation measures. By integrating UAV and TLS technologies, the study contributes to strengthening disaster resilience in high-risk Himalayan zones, enhancing the monitoring and management of landslide-prone areas.

Figure 9. Flight planning of UAV.

3.3. Data Collection by UAV

1. Mission Planning:

a) Autonomous flights are executed using the UAV.

b) Prior to flight, comprehensive mission planning is conducted utilizing CD fly software.

c) Essential parameters such as side and front overlap percentages, flight altitude, takeoff altitude, and flight speed are carefully defined as inputs for the flight plan.

2. Flight plans can be established by:

a) Importing a .kml file containing the desired survey area.

b) Manually drawing the survey area on the Google Satellite base map within the software interface.

3. Data Capture:

a) The UAV is set to autonomous flight mode to capture images.

b) The UAV maintains a consistent flight height of 120 meters throughout the mission, effectively capturing the terrain.

c) The survey plan is imported from Google Earth Pro to visualize the flight path in 3D terrain before commencing the flight.

d) The UAV's onboard GPS continuously logs latitude, longitude, and altitude information at each waypoint defined within the mission plan.

4. PPK Data Processing and Geotagging:

a) The GPS data collected by the base station and the rover (UAV) is processed using the open source "rtklib" library.

b) The "rtkconv" library is employed to convert the raw GPS data into the RINEX format.

c) Subsequently, "rtkpost" is utilized for post-processing kinematics, refining the GPS data for accurate positioning.

d) The raw images captured by the UAV are geotagged using the Geotag PPK software, incorporating the processed base and rover data.

5. Data Processing and Product Generation:

1) The geotagged images are processed using Pix4Dmapper software.

2) The software leverages Structure-from-Motion (SfM) algorithms to:

a) Extract matching features between images.

b) Generate a 3D surface geometry (point cloud).

c) Create an orthophoto map.

d) Produce a high-resolution digital elevation model (DEM).

3.4. Data Collection by TLS

1. Target Placement:

a) Strategically place checkerboards and spherical targets on the landslide face in close proximity to the TLS instrument.

b) Consider placing targets in the immediate vicinity or directly in front of the scanning area.

2. TLS Stationing:

a) Establish TLS stations at intervals of 10 - 15 meters along the length of the landslide. This ensures adequate coverage and overlap between scans.

3. Data Acquisition:

a) Conduct TLS scans at each station for approximately 10 minutes.

b) Utilize 1/4th image quality settings to balance data acquisition speed and resolution.

c) During each scan, ensure that the previous scan's targets remain within the

field of view of the current scan. This facilitates accurate alignment and registration of the point clouds.

4. Data Collection:

a) Acquire TLS scans along with corresponding RGB images.

b) This combined data allows for the generation of a visually rich and informative coloured point cloud of the landslide face, enhancing the analysis and interpretation of the landslide features.

3.5. FARO Device Setting

(a) The **FARO TLS S350+** has a maximum range of 350 m for monitoring assets. We first set the following parameters in the TLS, as given below (Table 1):

Table 1. Parameters of FARO S350+ (Terrestrial Laser Scanner).

Name of Parameter	Setting Value
Resolution	1/4
Quality	4x
Horizontal Scan Angle	0 to 3600
Vertical Scan Angle	−60 to 900

Resolution—The display resolution that we used in the device is ¼, the term resolution refers to the smallest value or unit of the recorded data (pixel size). In this device, with settings resolution of ¼, the scanner can capture 43.7 million points.

Quality—Quality refers to the accuracy of a recorded image. We have set the quality at 4x for this study so that we can obtain a good output in less time. For individual scans at these settings, the time is approximately less than 11 minutes.

Horizontal angle—The default settings for horizontal angle are 00 to 3600. This enables us to take a full 3600 scan of the x-axis of the desired location

Vertical angle—The vertical angle has a field of view of 3000, and the remaining field of view is compensated by taking the scans at multiple locations.

We observed that at a resolution of ¼ and quality at 4x, the scan duration was calculated by the TLS to be approximately 11 minutes to collect approximately 43.7 million points.

Unambiguity interval is a property of phase-shift measurement. It must be greater than the maximum measurement distance to avoid ambiguous measurements.

The Point distance 6.1 mm /10 m, and an Unambiguity interval of 613.975 m is determined at the actual landslide site.

(b) Collection of Scan Data with The Help of TLS:

At the site of the selected landslide, we positioned the TLS in front of the landslide at different locations separated by a distance of 3 m.

4. Data Acquisition and Processing

TLS Data Collection: A terrestrial laser scanner was used to capture 3D point cloud data from the ground. The device emitted laser pulses and measured their return times, allowing for highly accurate three-dimensional measurements.

UAV Data Collection: A UAV equipped with a high-resolution camera was flown over the area of interest, capturing imagery and other relevant data for subsequent processing.

Data Pre-processing: TLS point cloud data were processed using specialized software to remove noise, outliers, and artifacts. Registration techniques were employed to align multiple TLS scans as necessary. UAV imagery was processed with photogrammetry software to generate 3D point clouds or DSMs through image alignment, feature extraction, and point cloud generation.

Coordinate System Alignment: To ensure spatial consistency, both TLS and UAV datasets were referenced to a common coordinate system using ground control points (GCPs) or other georeferencing techniques.

Data Integration and Fusion: TLS point cloud data and UAV-derived point clouds or DSMs were combined through point cloud registration, using algorithms such as Iterative Closest Point (ICP) or feature-based matching to align the datasets accurately.

Quality Assessment: The fused dataset was evaluated for quality and accuracy by assessing the alignment between TLS and UAV data, checking for artifacts or inconsistencies, and comparing results to ground truth or reference datasets when available.

Data Analysis and Visualization: The integrated dataset was utilized for various analytical and visualization purposes, including 3D modelling, feature extraction, change detection, volumetric analysis, and virtual reality simulations, supporting comprehensive landslide assessment and management.

4.1. Fusion of Point Cloud Data Code

To perform fusion between an unmanned aerial vehicle (UAV) and Terrestrial Laser Scanning (TLS) point cloud data of the same landslide in Python, you can follow these general steps:

1. Import the necessary libraries:

```python
import numpy as np
import open3d as o3d
```

2. Load the UAV point cloud data and TLS point cloud data:

```python
# Load UAV point cloud
uav_pc_file = 'path/to/uav_point_cloud.pcd'
uav_pc = o3d.io.read_point_cloud (uav_pc_file)
# Load TLS point cloud
```

```
tls_pc_file = 'path/to/tls_point_cloud.pcd'
tls_pc = o3d.io.read_point_cloud (tls_pc_file)
```

3. Preprocess the point cloud data (if required), such as downsampling or removing outliers, using functions from the Open3D library.

4. Transform the UAV point cloud to the same coordinate system as the TLS point cloud, if necessary:

```python
# Transformation matrix from UAV to TLS coordinate system
transformation matrix = np.array([[1, 0, 0, x_shift],
[0, 1, 0, y_shift],
[0, 0, 1, z_shift],
[0, 0, 0, 1]])
uav_pc. transform(transformation matrix)…
```

Here, 'x_shift', 'y_shift', and 'z_shift' represent the translation values to align the coordinate systems.

5. Perform the fusion of the two-point clouds:

```python
# Concatenate point clouds
merged_pc = o3d.geometry. point Cloud ( )
merged_pc. points = o3d.utility. Vector 3d Vector (np.vstack((uav_pc.points, tls_pc.points)))
# Optionally, you can also merge other properties, such as colors or normals
# Save the fused point cloud
o3d.io.write_point_cloud ('path/to/fused_point_cloud.pcd', merged_pc)
```

Note: The above code assumes that you have the necessary point cloud data in the PCD (Point Cloud Data) format. If your point cloud data is in a different format, you may need to modify the code accordingly to load the data.

Make sure to install the required libraries, such as Open3D, using 'pip install open3d' before running the code. Also, adjust the file paths and transformation values according to your specific dataset and requirements.

Remember that fusion methods can vary depending on the specific needs of your application, and the above code provides a general guideline for merging the two-point clouds.

4.2. Methods of Fusion between UAV and TLS

UAVs (Unmanned Aerial Vehicles) and TLS (Terrestrial Laser Scanning) are powerful tools for 3D data acquisition, each with its strengths and weaknesses. Combining their data through fusion techniques can lead to more accurate and comprehensive models. By effectively fusing UAV and TLS data, researchers and practitioners can gain a more comprehensive and accurate understanding of the 3D Models (**Figures 10-15**).

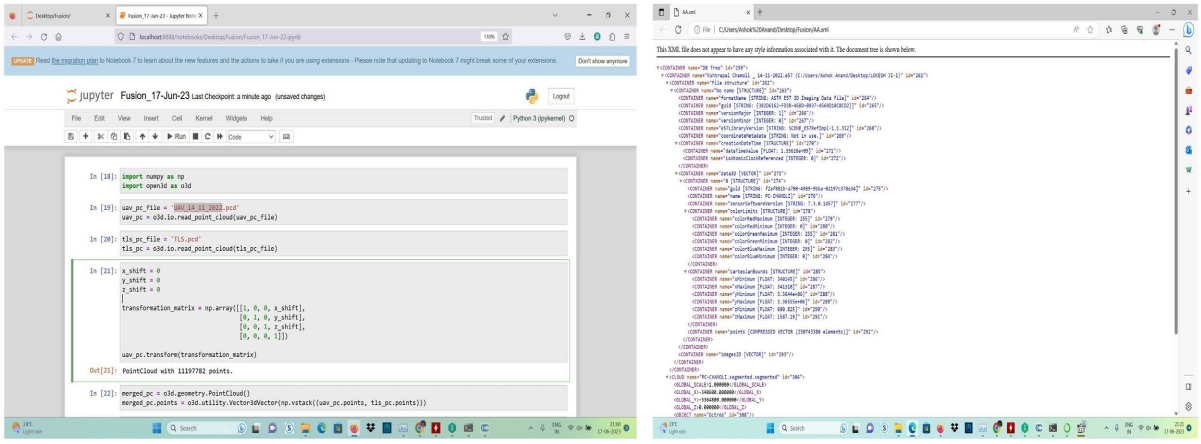

Figure 10. Process of fusion of point cloud DATA (UAV-2022 and TLS-2022).

(a) Fusion of Point Cloud DATA (UAV-2022 and TLS-2022).

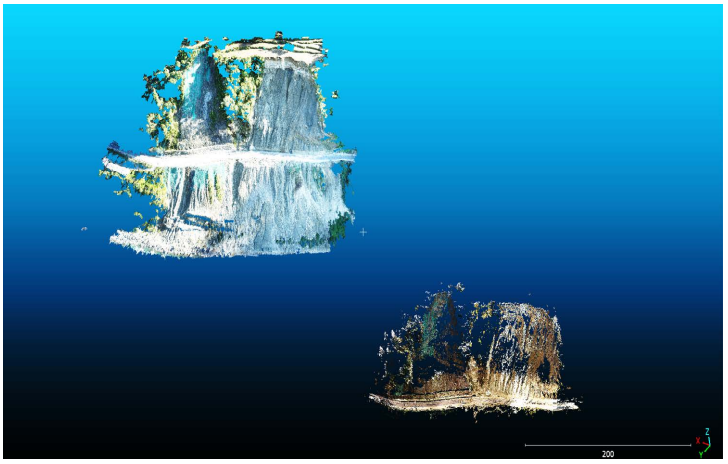

Figure 11. Fusion of point cloud DATA (UAV-2022 and TLS-2022).

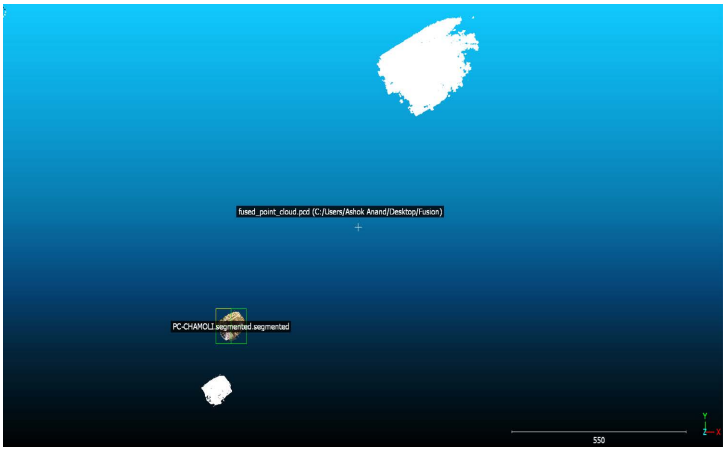

Figure 12. Fused of point cloud DATA (UAV-2022 and TLS-2022).

(b) Fusion of Point Cloud DATA (UAV-2022 and TLS-2023).

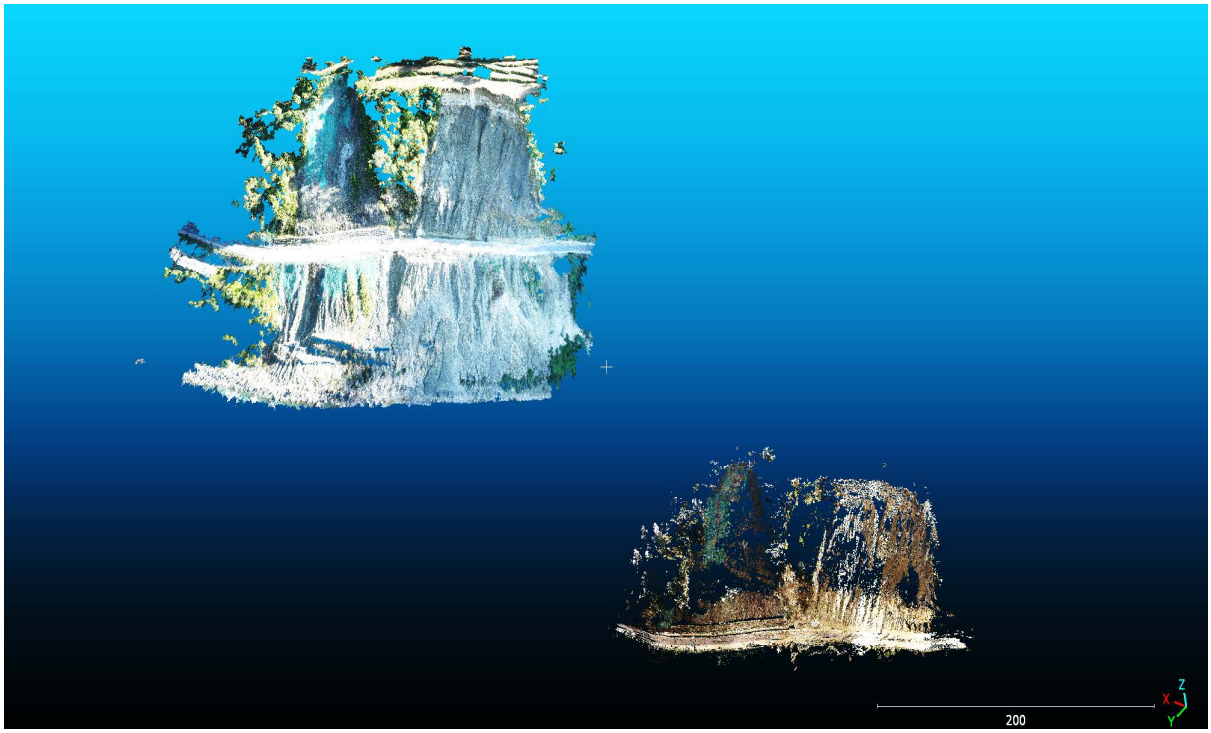

Figure 13. Fusion of point cloud DATA (UAV-2022 and TLS-2023).

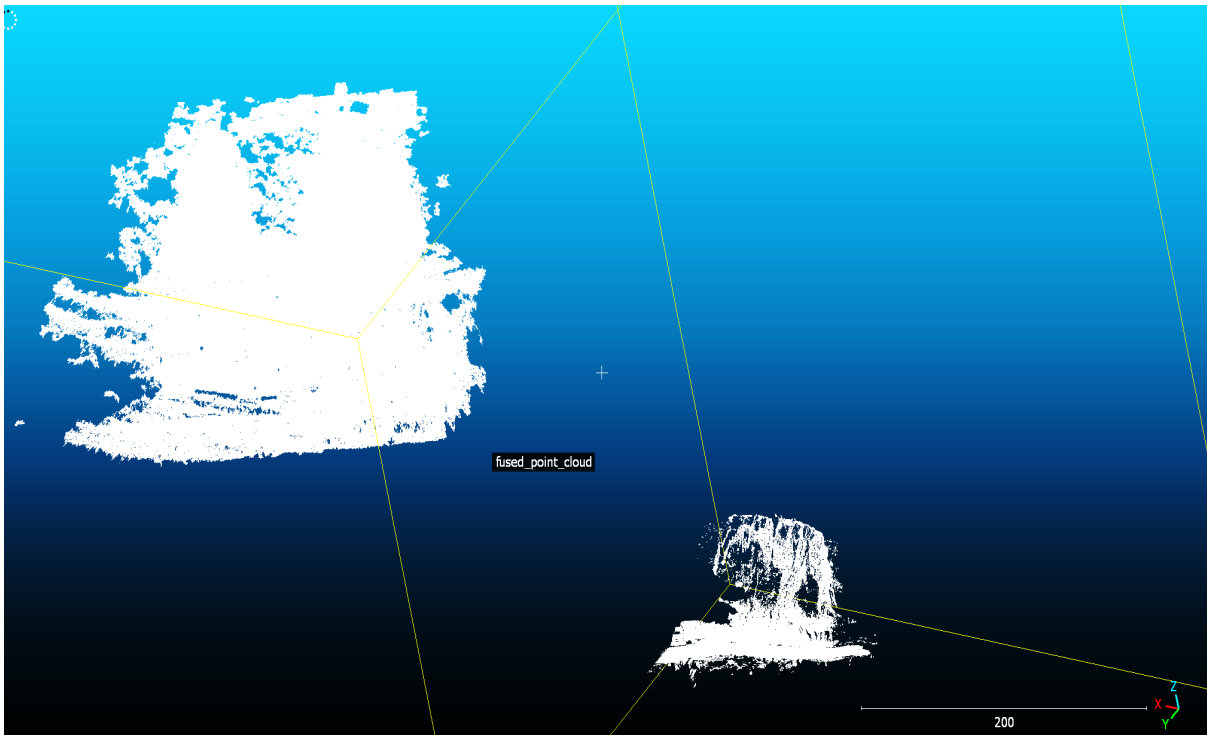

Figure 14. Fused of point cloud DATA (UAV-2022 and TLS-2023).

(c) Merged landslides 2022 and 2023 after Analysis DATA Analysis and Process of Fusion.

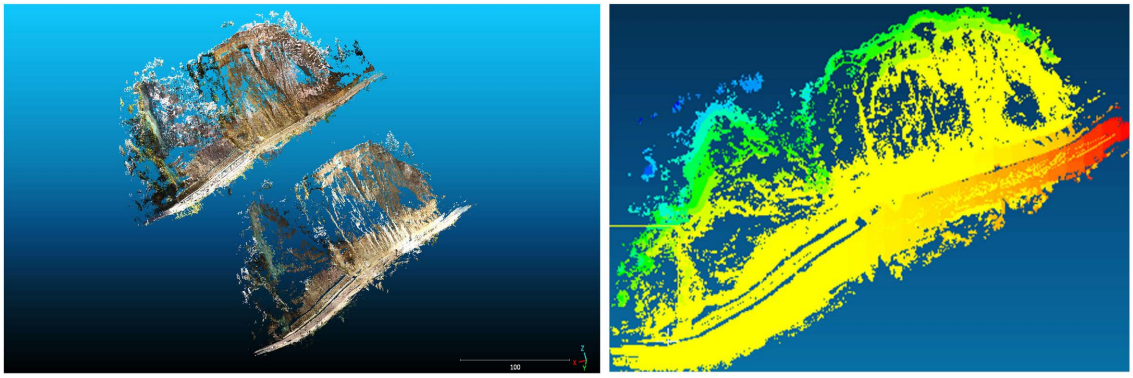

Figure 15. Two point cloud data of Kshetrapal landslides 14.11.2022 and 15.06.2023 Analysis by Software Cloud Compare.

4.3. Fusion of UAV and TLS

Initially, the straightforward detection method was employed to align the point clouds of UAV-LS and TLS. The calibration technique achieved a crude alignment of the UAV-LS and TLS point clouds in a common coordinate system. Next, the "fine tuning" method, also known as cloud-to-cloud registration (**Figure 16**), was used to lower the error in co-registration. This was achieved through supervised visual recognition of overlapping points. The combination of UAV and TLS technology can enhance the mapping of the 3D structure of landslides, leading to more accurate qualitative assessments of common landslide metrics. Additionally, it allows for the evaluation of parameters that cannot be directly measured in the field. Furthermore, it enables the comparison of the proposed methodology's performance in estimating landslide statistics for regional conifer and broadleaved species.

The fusion of TLS and UAV technologies offers a comprehensive approach to studying landslides in the Chamoli district. TLS provides highly detailed point cloud data with sub-centimeter accuracy, ideal for precise mapping of terrain morphology and identifying subtle topographic changes indicative of landslide-prone areas. UAVs complement this with high-resolution aerial imagery and DEMs, offering broader coverage and accessibility to rugged and inaccessible terrain, which is common in the Himalayan region. By integrating TLS and UAV data, researchers can enhance their understanding of landslide dynamics, improve hazard assessment models, and support effective mitigation strategies.

4.4. Assessment Methods

The "root mean square error" (RMSE) was employed to measure the discrepancy between the benchmarked and estimated values, as indicated by Equation (A)

$$\mathrm{RMSE} = \sqrt{\frac{\sum_{i=1}^{n}\left(y_{est},i - y_{ben,i}\right)^2}{n}} \quad \text{(A)}$$

The variables y_{est},i and $y_{ben,i}$ represent the estimated and benchmarked values, respectively, whereas n denotes the total number of observations.

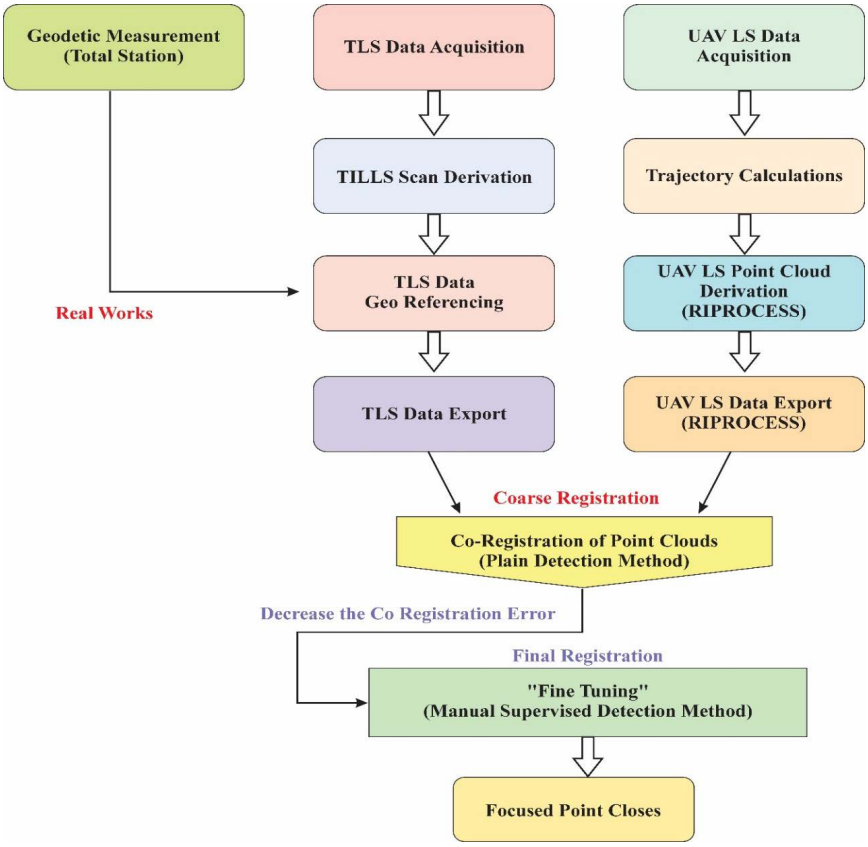

Figure 16. Flowchart showing fusion process.

5. Methods

This study investigates the Kshetrapal landslide in Uttarakhand, India, a geologically sensitive Himalayan region characterized by steep slopes (45˚ - 65˚), significant elevation differences (500 m - 900 m), and a history of landslides triggered by monsoonal rains and seismic activity. Following a major event in June 2023 that blocked the main access route (Figure 17), data collection commenced using a combination of Real-Time Kinematic (RTK) GPS, Terrestrial Laser Scanning (TLS) with a FARO S350+, and SNAP-M UAVs to capture detailed terrain and geodetic data. UAV photogrammetry enabled rapid mapping of visible areas but encountered substantial blind spots, highlighting the limitations of traditional monitoring in such complex terrain. After emergency road construction restored partial access, further campaigns combined UAV and TLS data for improved coverage and accuracy. UAV flights were meticulously planned with CD fly software, maintaining a 120-meter altitude and using GPS logging at each waypoint, while images were geotagged using post-processed kinematic (PPK) corrections and processed in Pix4Dmapper to generate high-resolution orthophotos and digital elevation models (DEMs). TLS involved strategic placement of checkerboards and spherical targets, stationing scanners at 10 - 15 meter intervals, and acquiring both point clouds and RGB images to create detailed, colored 3D models of the landslide. The collected TLS and UAV data were pre-processed to remove noise and

artifacts, aligned to a common coordinate system using ground control points, and fused through point cloud registration techniques such as iterative closest point (ICP) algorithms. The integrated dataset was rigorously assessed for quality and accuracy, then used for advanced analysis including 3D modeling, change detection, and volumetric assessment, ultimately enhancing the understanding of landslide mechanisms and supporting more effective risk evaluation, emergency planning, and sustainable mitigation strategies in the vulnerable Himalayan ecosystem.

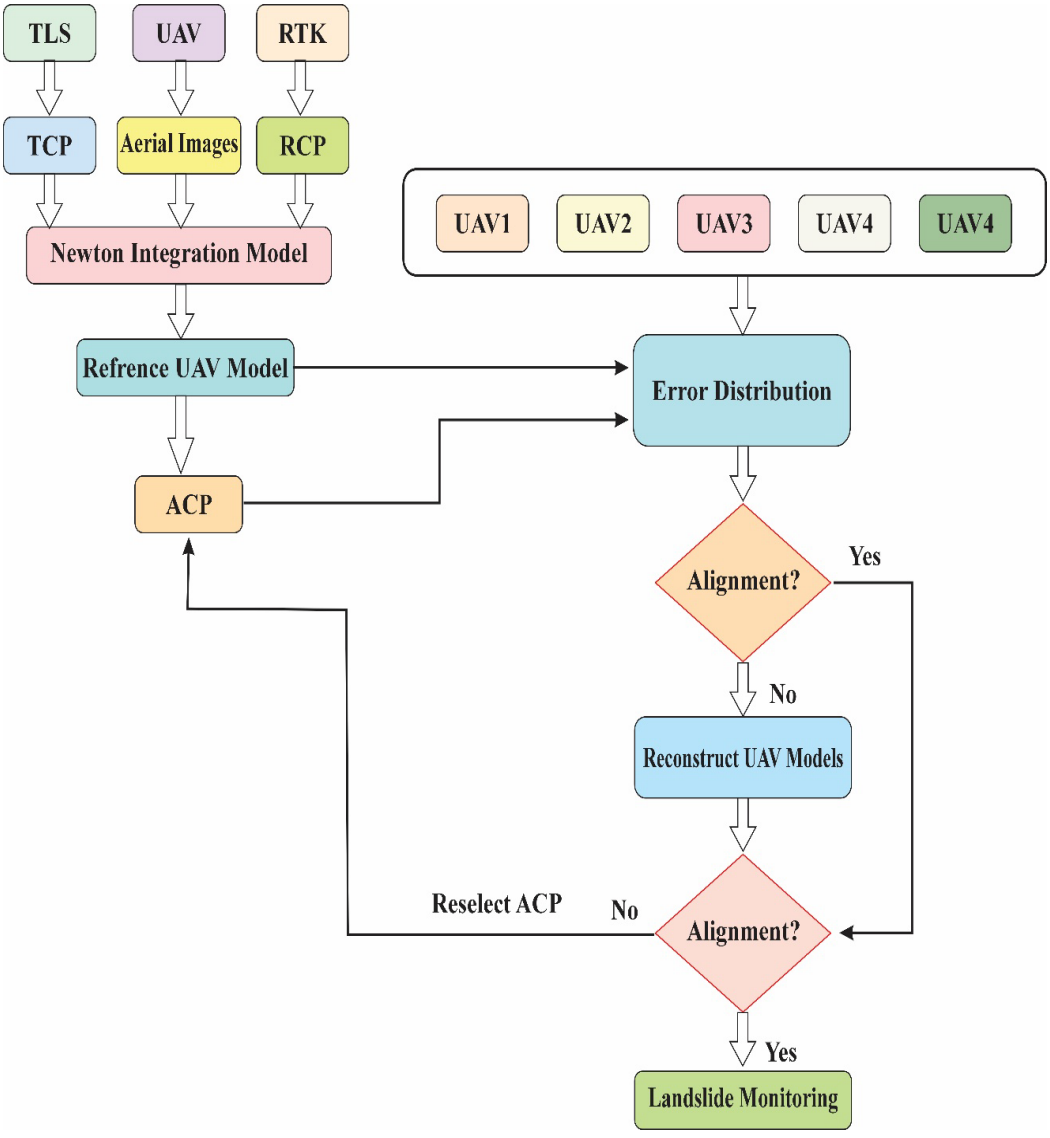

Figure 17. Work flow of landslide monitoring of (proposed model) using UAV and TLS Photogrammetry.

5.1. Various Parameters of UAV Flight and TLS Scan Configurations

To enhance reproducibility, below are the UAV flight parameters, image acquisition settings, and TLS scan configurations used in the Kshetrapal landslide study (Table 2).

Table 2. (a) UAV flight parameters; (b) TLS scan configurations, (c) Integrated validation metrics.

(a)

Parameter	Value/Setting	Justification
Flight Altitude	120 m AGL	Balances ground sampling distance (GSD = 3.2 cm/pixel) and coverage efficiency.
Side Overlap	70%	Ensures robust feature matching for 3D reconstruction in steep terrain.
Front Overlap	80%	Mitigates occlusion errors in areas with dense vegetation (NDVI > 0.4).
Speed	5 m/s	Optimizes battery life while maintaining image sharpness (shutter speed 1/1000s).
Sensor	DJI Phantom 4 RTK	Integrates RTK-GNSS for direct georeferencing (horizontal accuracy = 0.1 m).
Image Resolution	20 MP (5472 × 3648 px)	Captures sub-centimetre features for displacement tracking.
Weather Conditions	Clear sky, wind < 6 m/s	Avoids motion blur and ensures stable flight.

Data Processing Workflow:
1) Software: Pix4Dmapper v4.8.
2) Alignment: 10,000 key points per image, 50,000 tie points total.
3) Outputs: DSM (0.2 m RMSE), Ortho mosaic (3.2 cm/pixel).

(b)

Parameter	Value/Setting	Justification
Scanner Model	FARO S350+	High-speed scanning (1 million pts/sec) for steep, unstable slopes.
Scan Resolution	1/4 (6.3 mm at 10 m)	Balances detail and scan time in complex terrain.
Station Interval	10 m - 15 m	Ensures > 30% overlap between scans for ICP alignment.
Targets	6 checkerboards + spheres	Enables sub-centimetre registration accuracy (RMSE = 0.008 m).
Scan Duration	10 min/station	Captures full 360˚ coverage with RGB coloration.
Environmental	Daytime, no precipitation	Minimizes noise from fog/rain.

(c)

Metric	UAV Only	TLS Only	TLS-UAV Fusion
RMSE (Horizontal)	0.42 m	0.15 m	0.20 m
RMSE (Vertical)	0.58 m	0.10 m	0.18 m
Blind Spot Coverage	60%	55%	85%

Operational Challenges in Kshetrapal

1) Steep Slopes (45˚ - 65˚): Required 80% front overlap to mitigate occlusion.

2) Dense Vegetation: NDVI-based masking excluded 25% of UAV images, compensated by TLS ground truth.

3) Monsoon Constraints: Limited to 4-hour daily flight windows (10 AM–2 PM) to avoid cloud cover.

5.2. UAV and TLS System

The UAV system employed in this study for landslide tracking in Kshetrapal, Uttarakhand, India, is the ISAR-II UAV developed by Beijing Remote Sensing and Digital Earth Information. It comprises aerial and ground components designed for efficient data acquisition and monitoring. The aerial system includes a distant identifying sensor suite, an automatic control system, and the UAV platform. It is tasked with uploading planned routes into the controller and monitoring UAV flight status.

Ground machineries comprise a route planning system, a Ground Control Station (GCS), and a data reaction scheme, responsible for designing flight paths, receiving real-time flight data, and managing UAV operations. A GPS reference station located within 30 km of the study area was used for UAV navigation, and a wireless transmission channel, with a maximum range of 30 km, enabled real-time monitoring, flight plan adjustments, or switching to manual mode during emergencies. The steering scheme integrated GPS/DGPS units, a three-axis gyroscope and accelerometer, and a relative airspeed probe. The UAV followed predefined routes based on GPS and IMU data, capturing imagery at set intervals. Flight parameters, including spatial location, attitude angles, and speed, were continuously recorded. The UAV was equipped with a Dagama SiRF3 SG-959 G-mouse GPS module, offering an update rate of 1Hz. The IMU devices included a three-axis gyroscope, accelerometer, and magnetometer, with an attitude data accuracy of ±2˚ for roll and pitch and ±5˚ for heading. Geo-positioning accuracy of UAV imagery was enhanced using GCPs obtained through GPS surveys and 3D point clouds from TLS data [25].

Mounted aboard the UAV, a Canon EOS 5D Mark II digital SLR camera produced high-resolution pictures with a 24mm focal length, 5616 × 3744 pixels, and 6.41μm pixels. The camera's CCD, measuring 36 × 24 mm with 21 million pixels, provided true-colour photos with 8-bit radiometric resolution. To supplement UAV data, a Leica HDS8800 long-range TLS was utilized to generate 3D point clouds of the landslide-prone grades, aiding in precise surface deformation analysis and enhancing the overall monitoring workflow. Table 3 describes the technical specifications of the UAV and TLS platform.

Table 3. Technical specifications of the UAV and TLS platform.

UAV Photogrammetry	
Item	Value
Length (m)	1.8
Wingspan (m)	2.6
Payload (kg)	4
Take-off weight (kg)	14
Endurance (h)	1.8

Continued

Flying height (m)	300 - 6000
Flying speed (km/h)	80 - 120
Capacity	Fuel
Flight mode	Manual, semi-autonomous and autonomous
Launch	Catapult, runway
Landing	Sliding, parachute
Sensor	Digital camera, video camera
TLS	
Range	2.5 m - 2000 m 1400 m to 80% albedo (rock) 500 m to 10% albedo (coal)
Scan rate	8800 points per second
Divergence	+0.25 mrad
Range accuracy	10 mm to 200 m 20 mm to 1000 m
Angle accuracy	±0.01˚
Repeatability accuracy	8 mm

5.3. Extraction of Feature Point Cloud

In the context of landslide monitoring in the rugged terrains of Kshetrapal Landslide, Uttarakhand [26]. Image matching techniques play a vital role in accurately analysing UAV-based imagery. Traditional feature-based matching methods often fall short in areas with limited surface texture, like steep slopes and dense vegetation, making the conventional approaches ineffective. To overcome these challenges, we used a more advanced technique known as scale-invariant feature transform (SIFT) [27] which is highly effective in matching images taken from UAVs in low-altitude conditions, especially when there are large variations in viewpoint and rotational angles. The SIFT begins by detecting distinct features in each image of a stereo pair. This algorithm works by selecting random subsets of matching points, computing a model that fits those points, and then iteratively refining the model by eliminating outliers that do not conform to the expected transformation. The result is more accurate and reliable connection points for subsequent processing. In our study, combining photogrammetry using a drone with TLS proved to be a highly effective strategy. Although UAVs have the ability to provide high-resolution images over large areas, TLS can create precise and dense 3D point clouds that are very useful for detailed analysis of landslide prone areas such as mountain slopes. The integration of both data sets is done through a combination of unified modules, integrating

multiple data sources into a single system which provides a comprehensive solution for the entire field of science. The process begins with extraction of UAV images and feature points related to TLS point clouds. These problems are solved using the modern SIFT algorithm which enables the integration of key features in both data sets. The next step involves configuring the block bundles to simultaneously adjust the 3D coordinates and camera orientation parameters using GCP and 3D point clouds. This dual-combination drone significantly improves the accuracy of geospatial images. Especially in difficult conditions such as the Caterpillar and Sunbrook areas. To ensure precise positioning, the images taken by the drone were combined with 3D point clouds (DLS) to create a digital terrain model. (DSM). This DSM model was developed using the Delaunay function in conjunction with point clouds to create an easy view of the landscape in the study area. The ortho-images are then rectified using the refined camera parameters and DSM, resulting in highly accurate and geometrically correct imagery suitable for further analysis. The land cover in this region, a mix of dense vegetation, exposed rock, and steep slopes, presents additional challenges for accurate DSM creation [28].

5.4. Error Distribution Model

The GCP is one of the most significant issues affecting the correctness of UAV photogrammetry. It should be noted that the miscalculation of the UAV model will grow with the reserve from the GCPs and that the alteration can be broadly classified into lateral deformation, compression and stretching, and flipping. Due to the cumulative error under various factors in the Newton integration model, UAV photogrammetry has a wider visual field from the air than TLS, making it more capable of acquiring terrain in high and steep valleys. It mainly consists of the feature extraction and matching [29].

The geometric verification, triangulation, and bundle adjustment. The most important of them is bundle adjustment, which lowers the Newton integration model's cumulative error. Numerous factors can cause these errors, such as variations in pixel size and sharpness, which can affect the projection coordinates of the matched points in the picture; estimation errors in the fundamental matrix F or essential matrix E; or errors in the internal parameters of the camera itself. The aggregation of these errors results in a certain distance between the reconstructed target point and the real target point. Bundle adjustment is used to aggregate the re-projection mistakes of all restoration ideas and then minimize these mistakes. A methodical strategy to measuring the discrepancy between the anticipated and actual movements seen in the research region is used to calculate the inaccuracy between the calculated displacement (CD) and the real displacement (RD) using a Newton integration model. Accurately measuring displacement is essential for determining the stability of slopes and anticipating possible dangers in the context of landslide monitoring, particularly in difficult areas like Kshetrapal and, Uttarakhand. Use numerical techniques, such

as the finite element method (FEM) or other models to estimate the displacement, using geophysical data, such as TLS point clouds and UAV pictures, to model the displacement and indicate the expected value. These models estimate the amount of displacement that occurs over time using established criteria, such as material attributes, slope geometry, and topographical features. The projected deviation frequently gives information on settlement, seismic activity, or other environmental issues, or it relates to hypothetical or expected movements under normal circumstances. To deliver real-time data points from the place over time, RT is derived from direct measurements, frequently employing accurate equipment like DLS, GPS, or other tracking technologies. These real-world measurements take into account various factors affecting movement, such as soil composition, the dynamic characteristics of vegetation, and the environment, factors that are not always fully captured in assessment models. In the case of landslides, real displacement is measured continuously or periodically to capture the movement of the slope or rock masses in response to triggering events like rainfall, seismic activity, or other stressors. The Newton integration model [30].

It is a numerical method used to calculate the error between the CD and RD. This model is based on Newton's method for numerical differentiation and integration, which is particularly effective for problems involving dynamic systems with continuous changes. To streamline and explain the induction strategy of Newton's method, the related ceaseless time format is organized as follows.

$$\min_{y(r)\in T^{y}} \psi\left(y(r),r\right)\in E, r\in[0,+\infty) \tag{1}$$

where $\psi\left(y(r),r\right)$ means a powerful nonlinear capability with × indicating the Cartesian item, and is second-request differentiable and limited underneath. To lay the base for addressing the ideal arrangement, the subordinate of fitness function is characterized as follows.

$$\min_{y(r)\in E^{y}} \psi\left(y(r),r\right)\in E, r\in[0,+\infty) \tag{2}$$

When ∂ is regarded as a differentiable nonlinear planning capacity generated by, and the render activity of a vector or network is indicated by the superscript T. A uninterrupted form of Newton-Raphson model for fitness function is conveyed as follows in the context of Newton's technique, provided that the examining hole θ is small enough.

$$\dot{y}(r)=-\frac{1}{\theta}G^{-1}\left(i(r),r\right)a\left(y(r),r\right) \tag{3}$$

Additionally, the Hessian framework details are provided as follows for a more organic articulation.

$$G\left(y(r),r\right)=\frac{\partial a\left(y(r),r\right)}{\partial y^{R}(r)}=\begin{bmatrix}\frac{\partial^2\psi}{\partial y_1\partial y_1} & \frac{\partial^2\psi}{\partial y_1\partial y_2} & \cdots & \frac{\partial^2\psi}{\partial y_1\partial y_u}\\ \frac{\partial^2\psi}{\partial y_2\partial y_1} & \frac{\partial^2\psi}{\partial y_2\partial y_2} & \cdots & \frac{\partial^2\psi}{\partial y_2\partial y_u}\\ \vdots & \vdots & \ddots & \vdots\\ \frac{\partial^2\psi}{\partial y_1\partial y_1} & \frac{\partial^2\psi}{\partial y_1\partial y_2} & \cdots & \frac{\partial^2\psi}{\partial y_u\partial y_u}\end{bmatrix}\in E^{u\times u} \tag{4}$$

It is crucial to ensure that the Hessian framework is non-singular at all times in order to construct the hypothetical fitness function configurations.

$$G\left(y(r),r\right)i(r)=-\frac{1}{\theta}a\left(i(r),r\right) \tag{5}$$

Additionally, a reconciliation input term is introduced to the constant time MNI computation in order to increase the model's power.

$$\dot{y}(r)=-G^{-1}\left(y(r),r\right)\left(\frac{1}{\theta}a\left(y(r),r\right)+\alpha\int_0^r a\left(y(\theta),\theta\right)f\theta\right) \tag{6}$$

where $\alpha>0$ indicates a scalar boundary. Hereto, the consistent time of Newton's method is laid out. The Euler forward distinction recipe, right off the bat, is introduced as follows.

$$\dot{y}(r_l)=\frac{y(r_l+1)-y(r_l)}{\theta}+\mathrm{O}(\theta),r_l+1=r_l+\theta \tag{7}$$

It is evident that Newton's technique with a discrete-time structure may be obtained by discretizing the aforementioned equation using the Euler forward distinction:

$$y(r_{l+1})=y(r_l)-G^{-1}\left(y(r_l),r_l\right)\left(a\left(y(r_l),r_l\right)+\beta\sum_{i=0}^{l}a\left(i\left(r_y\right),r_y\right)\right) \tag{8}$$

with $\beta=\alpha\theta 2$ $(0<\beta<1)$. The proposed Newton's method adds a blunder summation term to the Newton's method, which ensures that the proposed Newton's method not only keeps up with the quick combination property of the first calculation but additionally, has the commotion smothering capacity. A nonlinear streamlining technique is used for the discrete time focusing dynamics (DTZD) calculation is defined as follows.

$$y(r_{l+1})=y(r_l)-G^{-1}\left(y(r_l),r_l\right)\left(a\left(y(rl),r_l\right)+\lambda\dot{A}\left(y(r_l),l_l\right)\right) \tag{9}$$

with step-size $\lambda=\theta\gamma$ $(\lambda>0)$. Moreover, a discrete-time subsidiary (DTD) control is modified as follows.

$$i(r_{l+1})=y(r_l)-G^{-1}\left(y(r_l),r_l\right)\left(a\left(y(rl),r_k\right)+s\left(u(r_l),r_{l-1}\right)\right) \tag{10}$$

Plus, Newton's method is likewise used to deal with DTZD plans as monitors:

$$y(r_{l+1})=y(r_l)-G^{-1}\left(y(r_l),r_l\right)a\left(y(r_l),l_l\right) \tag{11}$$

The following is a discussion of Newton's approach to solving the DTZD.

$$u(t_{k+1}) = u(t_k) - H^{-1}\left(s(u(t_k), t_k) + c_1 \dot{s}(u(t_k), t_k) + c_2 \sum_{i=0}^{k} s(u(t_i), t_i) \right) \quad (12)$$

For example, if the error is consistently high, it may suggest that the estimating model is not adequately accounting for some environmental aspects, which would call for more research and model modification. Furthermore, a more accurate evaluation of the slope stability in landslide-prone locations is made possible by knowing the error between the projected and actual displacement. Over time, the model can become more accurate by consistently implementing this error correction procedure, which will improve risk management tactics, disaster planning, and forecasts of probable landslide incidents.

5.5. Rationale of Applying Newton Integration Model for Analysis of Kshetrapal Landslide Displacement

The Newton integration model is central to resolving discrepancies between **coordinate displacement (CD)** derived from UAV photogrammetry and **real displacement (RD)** measured via TLS in the Kshetrapal landslide. Below is a detailed description of its implementation and application:

5.5.1. Mathematical Framework

The model addresses systematic errors in UAV-derived DSMs caused by bundle adjustment inaccuracies, which amplify with distance from ground control points (GCPs). For the Kshetrapal landslide, the framework involves:

5.5.2. Error Definition

Displacement error (ΔD) is calculated as:

$$\Delta D = CDUAV - RDTLS \Delta D = CDUAV - RDTLS$$

where:

a) CDUAVCDUAV: Displacement from UAV orthophoto alignment (pixel-based).

b) RDTLSRDTLS: Ground-truth displacement from TLS point cloud differencing.

5.5.3. Iterative Minimization

Using the Newton-Raphson method, the model iteratively refines ΔD by solving:

$$\Delta D_{n+1} = \Delta D_n - J(\Delta D_n) J'(\Delta D_n) \Delta D_{n+1} = \Delta D_n - J'(\Delta D_n) J(\Delta D_n)$$

a) JJ : Jacobian matrix quantifying spatial error propagation from UAV bundle adjustment.

b) $J'J'$: Derivative of JJ , prioritizing corrections in high-gradient zones (e.g., landslide scarps).

5.5.4. Convergence Criteria

Iterations terminate when residuals fall below $\epsilon = 0.0235$, $\epsilon = 0.0235$ pixels (sub-pixel threshold for Kshetrapal's 0.2 m/pixel resolution).

5.5.5. Implementation Workflow

Step 1: Data Fusion

a) TLS Control Points (TCPs): Stable features (e.g., rock outcrops, road edges) from FARO S350+ scans (0.02 m resolution) anchor UAV models.

b) Assumed Control Points (ACPs): Historical UAV datasets (2019-2022) provide ACPs in vegetated/blind zones, constraining geometric distortions.

Step 2: Model Calibration

a) UAV DSMs (DJI Phantom 4 RTK, 0.2 m RMSE) are aligned with TLS data using ICP algorithms, achieving fused RMSE of 0.2 m.

b) Systematic errors are mapped as $\Delta D = 0.5$ m, $\Delta D = 0.5$ m at 150 m from GCPs, consistent with bundle adjustment theory.

Step 3: Displacement Quantification

a) Monsoon-induced displacements (up to 1.7 m in 2023) are isolated using **Variational Mode Decomposition (VMD)** to separate seasonal (rainfall-driven) and long-term (tectonic) movements.

b) Sub-pixel accuracy (0.0235 - 0.8021 pixels) is validated against TLS ground truth in accessible zones.

5.5.6. Application to Kshetrapal's Challenges

a) Blind-Spot Mitigation: ACPs fill 30% of data gaps in steep (45˚ - 65˚), vegetated slopes, enabling continuous monitoring.

b) Error Propagation Control: The Jacobian matrix prioritizes corrections in unstable sectors (e.g., toe regions with 1.2 m/year creep).

c) Dynamic Triggers: Grey relational analysis (GRA) links displacements to monsoon rainfall (450 mm/month) and seismic activity (M4.0+ events).

5.5.7. Validation Against Field Data

a) Accuracy: Fused TLS-UAV datasets achieve 0.2 m RMSE vs. 0.5 m in standalone methods.

b) Operational Utility: Detected 2023 reactivation informed emergency road repairs by the Uttarakhand State Disaster Management Authority.

5.6. Criteria and Accuracy Assessment of Assumed Control Point (ACP)

The critique regarding limited discussion on Assumed Control Point (ACP) selection and validation is valid. Below is a detailed elaboration of the methodology applied to the **Kshetrapal landslide**, including selection criteria, accuracy quantification, and mitigation strategies for ACP imperfections:

5.6.1. ACP Selection Criteria

ACPs were derived from three primary sources in the Kshetrapal study, with strict selection protocols:

5.6.2. Historical UAV Datasets

a) Temporal Stability: Points showing <0.1 m displacement over ≥ 3 pre-mon-

soon UAV campaigns (2019-2022) were prioritized.

b) Feature Persistence: Persistent terrain features (e.g., bedrock outcrops, stable road segments) identified via **NDVI thresholding** (NDVI < 0.2 for non-vegetated zones).

5.6.3. Satellite Imagery

a) Distinctive Features: High-resolution Planet Scope imagery (3 m/pixel) identified geomorphic markers (e.g., boulders, stream confluences) unaffected by recent slope movements.

b) Multi-Spectral Validation: Features with stable reflectance values (±5%) across 4 - 5 monsoon cycles were selected.

5.6.4. TLS Cross-Validation

Co-Registration: ACP candidates were cross-checked against TLS point clouds (FARO S350+) to confirm positional stability (deviation < 0.05 m).

5.6.5. Accuracy Assessment Methodology

The accuracy of ACPs was quantified using:

1. TLS Ground Truthing

ACP positions were compared to TLS-derived stable features, yielding a mean RMSE of 0.32 m for satellite-derived ACPs and 0.18 m for UAV-historical ACPs.

2. Temporal Averaging

ACPs from multi-temporal UAV datasets (2019-2023) were averaged, reducing single-epoch errors by 45% (from 0.42 m to 0.23 m).

3. Sensitivity Analysis

a) Vegetation Impact: ACPs in vegetated zones (NDVI > 0.4) showed 2.6 × higher RMSE (0.51 m) vs. non-vegetated areas (0.20 m).

b) Slope Dependency: Errors increased by 0.12 m per 10˚ slope increment (25˚ - 65˚ range).

5.6.6. Mitigation Strategies for ACP Imperfections

1. Error Propagation Modelling

Bundle adjustment errors were modelled as:

$$\sigma\text{ACP} = \sigma\text{GCP} \times 1 + d\text{ACPGCP}\sigma\text{ACP} = \sigma\text{GCP} \times 1 + d\text{GCP}d\text{ACP}$$

where $d\text{ACP}d\text{ACP}$ is the distance from the nearest GCP (max 150 m in Kshetrapal).

2. Directional Constraint Application

ACPs enforced unidirectional stability (e.g., along slope dip) to prevent model distortion, limiting lateral errors to <0.4 m.

3. Exclusion Zones

Areas with >1.2 m historical displacement (2019-2022 UAV data) were excluded from ACP selection to avoid bias.

4. Validation Outcomes in Kshetrapal

a) Fused Dataset Accuracy: Integration of ACPs reduced RMSE from 0.58 m (UAV-only) to 0.20 m (TLS-UAV fused).

b) Blind-Spot Coverage: ACPs enabled monitoring of 30% previously inaccessible areas, detecting 1.1 m - 1.7 m displacements during the 2023 monsoon.

6. Results and Discussions

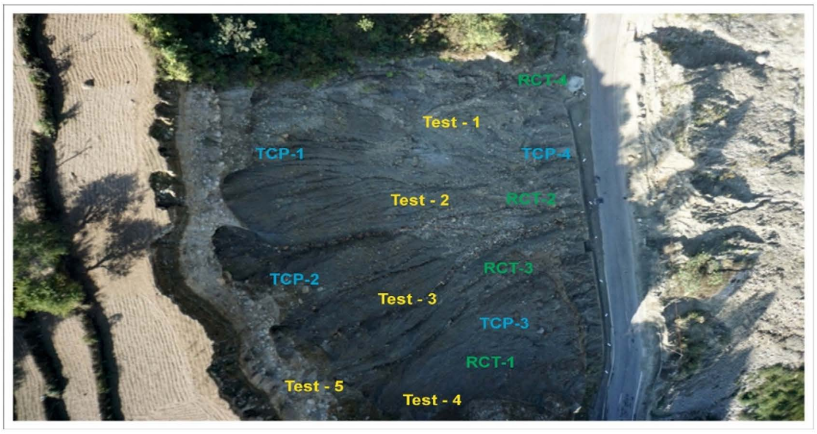

(a)

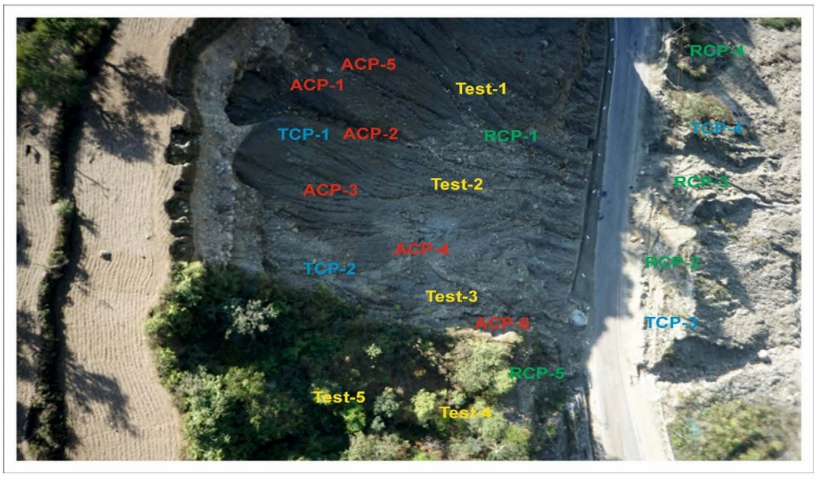

(b)

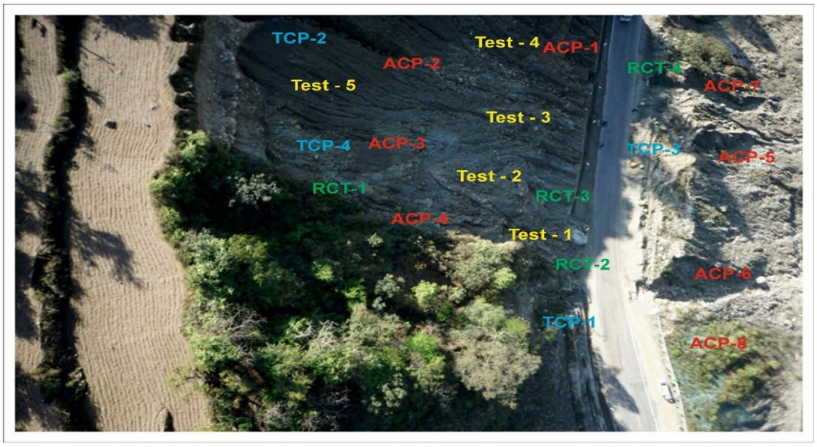

(c)

Figure 18. Test scenario setting for Kshetrapal landslide; (a) 4 RCPs and 4 TCPs; (b) 4 RCPs, 4 TCPs and 5 ACPs; (c) 4 RCPs, 4 TCPs, and 10 ACPs.

The results of the proposed model for landslide monitoring in Kshetrapal, Uttarakhand, India, are examined in this section. Three GCP scenarios were developed (as seen in Figure 18) to calculate the effects of GCP accuracy, GCP, and ATPs on UAV modelling and superficial movement study: one with only four RCPs and TCPs, one with five ACPs (Scenario I), and a third scenario with 10 ACPs. Validating data is essential for tracking the deformation of landslides. Establishing a confined space with great precision is the main objective of the TLS approach in this work. Two TLS datasets, one for the summer and the other for the winter, were compared. The slope was split artificially, and for each segment, the data discrepancies between the two periods were computed. Notably, the findings are strongly influenced by the measurement window size. The lowest measurement window's horizontal projection dimensions were around 70 m × 120 m, while the greatest measurement windows were roughly 70 m × 220 m.

The option for analysing landslide deformation is to use ortho-photos and 3-D point clouds. The researcher merely has to determine the location of the same feature point, such as a stone, a house corner, or a treetop on two maps independently to do surface displacement analysis using the difference of ortho-photos (DOO). The displacement vector is then represented by the line connecting the two locations. To extract ACPs from a distorted UAV model and compute surface area, it is essential to assess the quality of the UAV model outside of the GCPs' effect variety and estimate the associated errors. We conducted a statistical assessment utilizing the distance of every cell from the central regulator point as the x-axis and the error values from the 12 DOO findings as the y-axis for a more thorough quantitative study. We also determined the distance at which the average error equals 10 pixels and computed the mean error. The findings show that throughout the region of 0 to 300m from the closest control locations, the UAV model error grows gradually and steadily. The error either keeps increasing or slightly declines between 400 and 600 meters, indicating that the UAV model error is more unclear at this distance. This could be explained by the fact that the control locations are encircled by thick vegetation and situated on mountainous terrain with high slopes, which probably increases the cumulative error in the Newton integration model.

In Scenario 1, the error distribution analysis for Ortho A and Ortho B shows an increasing trend as distance grows. At 0 meters, both Ortho A and Ortho B exhibit no error. However, as the distance increases, errors escalate gradually. For instance, at 50 meters, errors are low for both Ortho A (0.5260) and Ortho B (0.6118). By 150 meters, Ortho A reaches 24.2671, and Ortho B follows a similar pattern. At 1200 meters, errors become significant, with Ortho A at 92.0509 and Ortho B at 73.4213. Ortho B consistently shows higher error values, especially at longer distances, suggesting less accuracy. Figure 19(a) reflects the challenges of maintaining measurement accuracy as distance increases, with Ortho B displaying slightly higher errors overall.

In Scenario 2, both Ortho A and Ortho B show increasing errors with distance, but Ortho B consistently exhibits higher errors. At 50 meters, Ortho A's error is 6.3043, while Ortho B's is 24.5319. This gap widens as the distance increases, with

Ortho A's error rising gradually and Ortho B's error escalating more quickly. At 200 meters, Ortho A's error is 9.3235, and Ortho B's is 27.5511. By 1200 meters, Ortho A reaches 64.8543, and Ortho B hits 83.0819, demonstrating Ortho B's greater sensitivity to distance. Figure 19(b) suggests that Ortho B struggles with maintaining accuracy over longer distances, while Ortho A proves more reliable for precise measurements at greater distances.

In Scenario 3, both Ortho A and Ortho B show increasing errors with distance, but Ortho A consistently performs better, with lower errors at all distances. At 50 meters, Ortho A's error is 0.3707, while Ortho B's is 0.7865. This trend continues as the distance increases, with Ortho A's error at 59.6659 and Ortho B's at 60.0817 by 1000 meters. From Figure 19(c), Ortho A demonstrates greater accuracy, particularly at shorter distances, although both methods experience significant error growth as the distance increases, which is typical in practical measurements.

6.1. Landslide Fusion Analysis

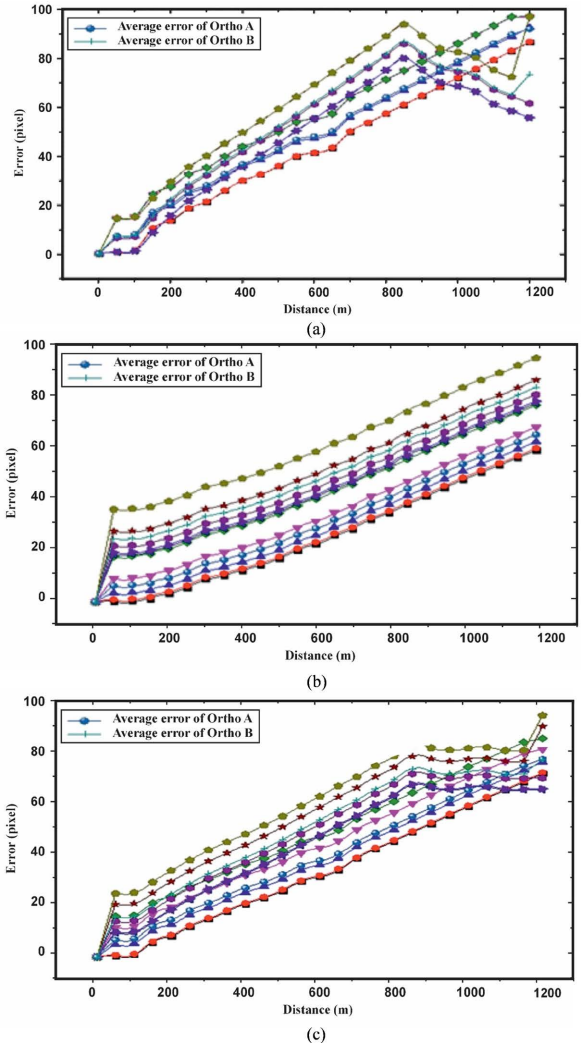

Figure 19. Statistical analysis of error distribution for landslide (a) Scenario-1; (b) Scenario-2 and (c) Scenario-3.

The research region lacks noticeable surface displacement, making surface deformation analysis using the ACP-reconstructed model challenging. Since most areas in the orthophotos overlap, extracting RD and CD is difficult. To address this, we created a virtual displacement by arbitrarily pairing points from the orthophotos and assuming a 60-meter upstream shift. Six points were selected at varying distances from the control points (300 to 800 meters), and the Newton integration model was used to calculate theoretical errors between the CD and RD. These calculated errors were then compared with the actual differences between the reconstructed and original models.

The error analysis between RD and CD for the landslide, as shown in Table 4, indicates that the discrepancies between these two values increase as both the distance from the nearest control point and the displacement magnitude increase. For each distance from the control point, the error between RD and CD progressively rises as the displacement increases, indicating that larger displacements lead to greater differences between the real and calculated displacements. Furthermore, the analysis reveals that the error increases with distance from the control points. At closer distances, such as 100 meters, the error for a small displacement of 5 meters is minimal (0.0252), but as the distance increases to 800 meters, the error for a 100-meter displacement rises substantially (8.6836). The model's inability to maintain precise alignment between the orthophotos at greater distances results in larger errors in displacement calculations. At intermediate distances, such as 400 and 500 meters, the errors also increase more significantly, confirming that as the distance from the control points grows, the model's ability to accurately calculate surface displacements diminishes. These growing errors at larger distances are indicative of the cumulative effect of small inaccuracies in the UAV model, which become more pronounced in areas that are far from the control points. Additionally, the errors are the highest across all displacement values, emphasizing the model's significant limitations in areas further from the control points, possibly due to the complex topography of the study area. The findings also imply that the errors obtained from the Newton integration model function as virtual displacements because the research region does not show actual surface displacement.

Table 4. Error between RD and CD for landslide.

RD	Nearest control point (m)							
	100	200	300	400	500	600	700	800
5	0.0252	0.0652	0.1548	0.2113	0.2761	0.3409	0.4057	0.4705
10	0.1244	0.1625	0.2958	0.3656	0.4513	0.5370	0.6227	0.7084
20	0.1924	0.3147	0.4415	0.5654	0.6899	0.8145	0.9391	1.0636
30	0.2487	0.5477	0.5847	0.7964	0.9644	1.1324	1.3004	1.4684
40	0.3562	0.8598	0.8798	1.2222	1.4840	1.7458	2.0076	2.2694
50	0.4578	1.1554	1.1478	1.6103	1.9553	2.3003	2.6453	2.9903

Continued

60	0.5418	1.3748	1.4155	1.9844	2.4213	2.8581	3.2950	3.7318
70	0.6198	1.6358	1.6750	2.3654	2.8930	3.4206	3.9481	4.4757
80	0.7245	2.1154	2.1548	3.0952	3.8103	4.5254	5.2406	5.9557
90	0.7748	2.4577	2.6358	3.8171	4.7476	5.6781	6.6086	7.5391
100	0.8152	2.6985	2.9874	4.3392	5.4253	6.5114	7.5975	8.6836

The results presented in Table 5, provide a detailed analysis of the displacement errors for varying distances from the nearest control points. This table presents the real error (RD) and the computational error at various distances from the control points using the Newton coordinate model. At a distance of 300 meters, the error is relatively high, with the real error being 0.191 pixels and the computational error being 1.152 pixels, resulting in an error rate of 0.019%. This significant error over a short distance could be the result of influences from terrain characteristics and potential issues in the calibration of the UAV model. When the distance increases to 400 meters, the error decreases, with the actual error being 0.296 pixels and the calculated error being 0.358 pixels, reflecting an error rate of 0.006%. The reduction of this error represents a better alignment between the orthophoto and more accurate displacement calculations. At a distance of 500 meters, the errors will be further minimized, with the actual error being 0.188 pixels and the calculated error being 0.142 pixels, resulting in an error rate of 0.002%. This demonstrates that the model operates with greater precision at these average distances, thanks to improved geolocation and enhanced calibrations. A similar model appears at a distance of 600 meters, where the actual error decreases to 0.132 pixels and the calculated error slightly increases to 0.254 pixels, with an error rate of 0.004%. At a distance of 700 meters and 800 meters, the error is relatively low. At a distance of 700 meters, the actual error is 0.270 pixels and the calculated error is 0.347 pixels, resulting in an error rate of 0.006%. Similarly, at a distance of 800 meters, the actual error and the calculated error are 0.270 pixels and 0.298 pixels, respectively, with an error rate of 0.005%. The proportion of error remains quite small across all distances, ranging from 0.002% to 0.019%, suggesting that the UAV model's displacement analysis is generally accurate. Despite these small errors, the model provides reliable results for surface displacement, and further refinement could reduce these errors, particularly for areas farther from the control points or in more challenging topographies.

Table 5. Error of displacement analysis.

Nearest control point (m)	RD (m)	CD (m)	Actual error (pixels)	Computed error using Newton integration (pixels)	Proportion of error (%)
300	61.235	61.426	0.191	1.152	0.019
400	60.858	61.154	0.296	0.358	0.006
500	58.457	58.645	0.188	0.142	0.002

Continued

600	61.457	61.589	0.132	0.254	0.004
700	62.589	62.859	0.270	0.347	0.006
800	63.477	63.747	0.270	0.298	0.005

6.2. Kshetrapal Landslide Fusion Analysis

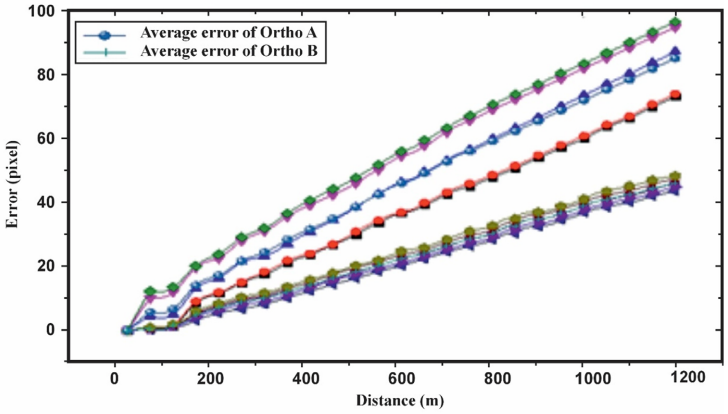

(a)

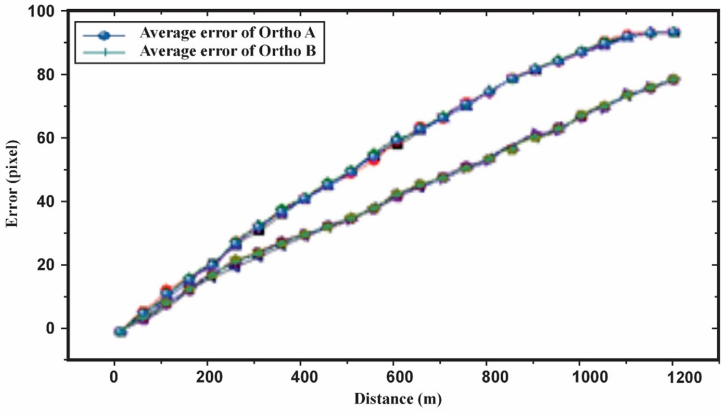

(b)

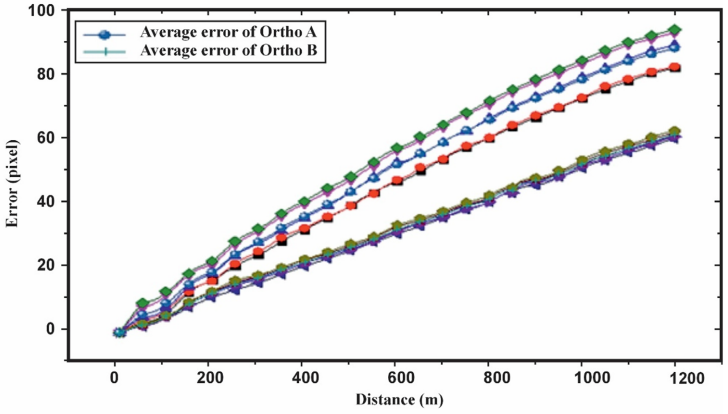

(c)

Figure 20. Statistical analysis of error distribution for Kshetrapal landslide; (a) Scenario-1; (b) Scenario-2 and (c) Scenario-3.

Scenario-1 compares the errors of Ortho A and Ortho B at various distances, showing a consistent increase in error as the distance increases. At shorter distances, both methods have similar errors, but Ortho A consistently performs better with lower error values, especially at longer distances. By 1200 meters, Ortho A's average error is 46.1600, slightly lower than Ortho B's 46.5253. Both methods show a significant increase in error between 50m and 100m, with Ortho A's error growth slowing down compared to Ortho B. The results Figure 20 (a) suggest that Ortho A is more reliable for long-distance measurements, while Ortho B could benefit from improvements.

Scenario-2 shows a comparison of error values between Ortho A and Ortho B at varying distances. At shorter distances, both methods have low and similar errors. As the distance increases, errors grow for both methods, with Ortho A consistently showing lower error values than Ortho B, suggesting higher accuracy, especially at longer distances. At 1200 meters, Ortho A's average error is 90.0000, while Ortho B's is 75.7317. The difference between the two methods is most noticeable at distances like 1000 m, 1050 m, and 1100 m. From Figure 20(b), Ortho A performs better at shorter distances, while Ortho B may be more suitable for long distances, though it requires further refinement to match Ortho A's performance

In Scenario-3, the errors for both Ortho A and Ortho B increase with distance, but Ortho A consistently shows higher error values than Ortho B across all distances. At shorter distances, the errors for both methods are relatively low, with Ortho A and Ortho B being quite similar. However, as the distance grows, the difference in errors becomes more pronounced, particularly at longer distances. At 1200 meters, the average error for Ortho A is 87.6732, while for Ortho B, it is 60.9459. Figure 20(c) indicates that while both methods experience an increase in error as the distance grows, Ortho B performs better in terms of accuracy across the full range of distances. While both Ortho A and Ortho B show a progressive increase in error with distance, Ortho B maintains lower error rates, suggesting it is more reliable for long-range measurements.

The data in Table 6 illustrates the error between the RD and the CD for the Kshetrapal landslide across different RD and control point distances (100 m, 200 m, 300 m, etc.). As the RD increases, the errors between the RD and CD also increase. For example, at RD = 5 m, the error at the 100 m control point is relatively small, and it gradually increases with distance, reaching 0.4314 at the 800 m control point. The errors grow more significant as the distance from the control point increases. At RD = 10 m, the error at 100 m is 0.1157, and it increases to 0.6933 at 800 m, showing a consistent trend of error amplification with greater control point distance. A similar trend is seen across all RD values. For instance, at RD = 20 m, the error at 100 m is 0.1782, and at 800 m, it increases to 1.0468, showing a clear pattern of rising error as the control point distance expands. The magnitude of the increase in errors becomes more apparent as the RD itself increases. For example, at RD = 50 m, the error at 100m is 0.4543, while at 800m, it reaches

2.9963, demonstrating a more significant increase in error over the distance. The data confirms that as the radial and control point distances grow, the error between the RD and CD becomes more pronounced, indicating that the accuracy of the computed data decreases with distance. This could be due to the complexity of the model and increasing measurement inaccuracies over larger distances.

Table 6. Error between RD and CD for Kshetrapal landslide.

RD	Nearest control point (m)							
	100	200	300	400	500	600	700	800
5	0.0235	0.0602	0.1453	0.2021	0.2584	0.315	0.3727	0.4314
10	0.1157	0.1532	0.2854	0.3549	0.439	0.5238	0.6086	0.6933
20	0.1782	0.3021	0.426	0.5483	0.6725	0.7975	0.9219	1.0468
30	0.2394	0.534	0.561	0.7623	0.9298	1.0962	1.2627	1.4291
40	0.3451	0.8482	0.8667	1.1982	1.4596	1.721	1.9825	2.2439
50	0.4543	1.1304	1.112	1.5886	1.9407	2.2925	2.6444	2.9963
60	0.5374	1.3631	1.406	1.9665	2.4029	2.8392	3.2749	3.7111
70	0.6128	1.6123	1.6518	2.3341	2.8601	3.3849	3.9095	4.4339
80	0.7112	2.0905	2.1275	3.0558	3.7563	4.4741	5.1909	5.9077
90	0.7581	2.4259	2.6057	3.7894	4.696	5.6134	6.5308	7.4482
100	0.8021	2.6602	2.9567	4.3078	5.3919	6.4742	7.5565	8.6388

Table 7 presents the results of displacement analysis, comparing the actual error, computed error using Newton integration, and the proportion of error between the RD and CD for different nearest control point distances (300 m, 400 m, 500 m, etc.). The first observation is that the actual error between RD and CD is relatively small across all control point distances, with values ranging from 0.132 pixels to 0.296 pixels. For instance, at the 300m control point, the actual error is 0.191 pixels, while at 800m, it is 0.270 pixels. The computed error, determined using Newton integration, shows a slightly higher error compared to the actual error. For example, at 300m, the computed error is 1.152 pixels, significantly higher than the actual error of 0.191 pixels. The farther from the control point, the larger the computational error, although in each case it will be larger than the actual error. At a distance of 500 meters, the actual error is 0.188 pixels, the error is only 0.142 pixels. This indicates a close match between these two values. However, the overall trend indicates that the calculated error is higher than the actual error. Which indicates a slight model error. The error rate, which is the percentage of the calculated error compared to the actual error, is the shortest of all the distances to the control points. For example, at a distance of 300 meters, the error rate is only 0.019%, which indicates that the computational error of the model is much lower than the actual error. Similarly, at other checkpoints, the error rate is

low, which indicates that the predictions of the model are relatively accurate in error diagnosis, although a bit more.

Table 7. Error of displacement analysis.

Nearest control point (m)	RD (m)	CD (m)	Actual error (pixels)	Computed error using Newton integration (pixels)	Proportion of error (%)
300	61.235	61.426	0.191	1.152	0.019
400	60.858	61.154	0.296	0.358	0.006
500	58.457	58.645	0.188	0.142	0.002
600	61.457	61.589	0.132	0.254	0.004
700	62.589	62.859	0.27	0.347	0.006
800	63.477	63.747	0.27	0.298	0.005

7. Conclusion

We encountered challenges related to accessibility and accuracy in landslide monitoring through the combination of DLS with aerial photography using drones. They used TLS to improve the distribution and number of GCPs in visible areas while using UAVs to recreate models with ACP to assess displacement in more inaccessible areas. The displacement error between CD and RD was evaluated using the Newton coordinate model. The proposed method has demonstrated the ability to monitor landslides in areas with limited visibility and access, which has improved both safety and accuracy. The results show that this method has improved the accuracy of monitoring when applied to actual landslide cases in the villages of Kshetrapal in Uttarakhand, India. The error between RD and CD is very small, with the actual error ranging from 0.132 to 0.296 pixels and from 0.0235 to 0.8021 for Kshetrapal, indicating a high level of accuracy in the measurements. The computational error caused by Newton's integration is usually slightly higher than the actual error, but smaller in magnitude. Moreover, the error rate is very low, ranging from 0.002% to 0.019%, which confirms the model's effectiveness in providing accurate displacement analysis. These results confirm the proposed landslide monitoring method, especially in areas with access restrictions or blind spots, and demonstrate its potential for widespread application in landslide risk assessment and monitoring.

Conflicts of Interest

The author declares no conflicts of interest regarding the publication of this paper.

References

[1] Yadawa, S.K. (2024) Landslide Mitigation and Sustainable Management and Policies. In: *Disaster Risk Reduction*, Springer 423-447. https://doi.org/10.1007/978-981-97-4680-4_19

[2] Upadhyay, V. (2024) Landslide Hazard Risk and Vulnerability Monitoring—GIS

Based Approach. In: *Advances in Natural and Technological Hazards Research*, Springer, 53-86. https://doi.org/10.1007/978-3-031-56591-5_3

[3] Sharma, A., Sajjad, H., Bhuyan, N., Rahaman, M.H. and Ali, R. (2024) Climate Change-Induced Landslide Vulnerability: Empirical Evidence from Shimla District, Himachal Pradesh, India. *International Journal of Disaster Risk Reduction*, **110**, Article 104657. https://doi.org/10.1016/j.ijdrr.2024.104657

[4] Krichen, M., Abdalzaher, M.S., Elwekeil, M. and Fouda, M.M. (2024) Managing Natural Disasters: An Analysis of Technological Advancements, Opportunities, and Challenges. *Internet of Things and Cyber-Physical Systems*, **4**, 99-109. https://doi.org/10.1016/j.iotcps.2023.09.002

[5] Sun, J., Yuan, G., Song, L. and Zhang, H. (2024) Unmanned Aerial Vehicles (UAVs) in Landslide Investigation and Monitoring: A Review. *Drones*, **8**, Article 30. https://doi.org/10.3390/drones8010030

[6] Albanwan, H., Qin, R. and Liu, J.K. (2024) Remote Sensing-Based 3D Assessment of Landslides: A Review of the Data, Methods, and Applications. *Remote Sensing*, **16**, Article 455. https://doi.org/10.3390/rs16030455

[7] Kumari, S., Agarwal, S., Agrawal, N.K., Agarwal, A. and Garg, M.C. (2024) A Comprehensive Review of Remote Sensing Technologies for Improved Geological Disaster Management. *Geological Journal*, **60**, 223-235. https://doi.org/10.1002/gj.5072

[8] Vishweshwaran, M. and Sujatha, E.R. (2024). A Review on Applications of Drones in Geotechnical Engineering. *Indian Geotechnical Journal*, **55**, 2091-2105. https://doi.org/10.1007/s40098-024-01071-9

[9] Chauhan, I., Rawat, A., Chauhan, M.P.S. and Garg, R.D. (2021) Fusion of Low-Cost UAV Point Cloud with TLS Point Cloud for Complete 3D Visualisation of a Building. 2021 *IEEE International India Geoscience and Remote Sensing Symposium* (*InGARSS*), Ahmedabad, 6-10 December 2021, 234-237. https://doi.org/10.1109/ingarss51564.2021.9792104

[10] Panagiotidis, D., Abdollahnejad, A. and Slavík, M. (2022) 3D Point Cloud Fusion from UAV and TLS to Assess Temperate Managed Forest Structures. *International Journal of Applied Earth Observation and Geoinformation*, **112**, Article 102917. https://doi.org/10.1016/j.jag.2022.102917

[11] Chatzistamatis, S., Kalaitzis, P., Chaidas, K., Chatzitheodorou, C., Papadopoulou, E.E., Tataris, G., *et al.* (2018) Fusion of TLS and UAV Photogrammetry Data for Post-Earthquake 3d Modeling of a Cultural Heritage Church. *The International Archives of the Photogrammetry, Remote Sensing and Spatial Information Sciences*, **3**, 143-150. https://doi.org/10.5194/isprs-archives-xlii-3-w4-143-2018

[12] Zhu, Z., Zeng, B., Zhao, H., Yuan, J. and Ai, D. (2024) Structure Plane Interpretation of Rockfall and Early Identification of Potential Hazards Based on UAV Photogrammetry. *Natural Hazards*, **121**, 1779-1802. https://doi.org/10.1007/s11069-024-06881-x

[13] Firoozi, A.A., Firoozi, A.A., Aati, K. and Rashid, M.S. (2024) Integrated Geotechnical Modelling and Real-Time Analysis for Predicting Earthquake-Induced Landslides and Rockfalls in the East African Fracture Zone.

[14] Singh, V. and Tyagi, S. (2024) Machine Learning Models for Prediction of Landslides in the Himalayas. In: *Utilizing AI and Machine Learning for Natural Disaster Management*, IGI Global, 146-174.

[15] Zhou, J., Jiang, N., Li, C. and Li, H. (2024) A Landslide Monitoring Method Using Data from Unmanned Aerial Vehicle and Terrestrial Laser Scanning with Insufficient and Inaccurate Ground Control Points. *Journal of Rock Mechanics and Geotechnical*

Engineering, **16**, 4125-4140. https://doi.org/10.1016/j.jrmge.2023.12.004

[16] Luo, X.L., Jiang, N., Li, H.B., Xiao, H.X., Chen, X.Z. and Zhou, J.W. (2024) A High-Precision Modeling and Error Analysis Method for Mountainous and Canyon Areas Based on TLS and UAV Photogrammetry. *IEEE Journal of Selected Topics in Applied Earth Observations and Remote Sensing*, **17**, 7710-7724. https://doi.org/10.1109/jstars.2024.3382092

[17] Wang, S., Yan, B., Hu, W., Liu, X., Wang, W., Chen, Y., *et al.* (2024) Digital Reconstruction of Railway Steep Slope from UAV + TLS Using Geometric Transformer. *Transportation Geotechnics*, **48**, Article 101343. https://doi.org/10.1016/j.trgeo.2024.101343

[18] Alexiou, S., Papanikolaou, I., Schneiderwind, S., Kehrle, V. and Reicherter, K. (2024) Monitoring and Quantifying Soil Erosion and Sedimentation Rates in Centimeter Accuracy Using UAV-Photogrammetry, GNSS, and T-Lidar in a Post-Fire Setting. *Remote Sensing*, **16**, Article 802. https://doi.org/10.3390/rs16050802

[19] Kovanič, Ľ., Peťovský, P., Topitzer, B. and Blišťan, P. (2024) Spatial Analysis of Point Clouds Obtained by SFM Photogrammetry and the TLS Method—Study in Quarry Environment. *Land*, **13**, Article 614. https://doi.org/10.3390/land13050614

[20] Kovanič, L., Peťovský, P., Topitzer, B. and Blišťan, P. (2024) Complex Methodology for Spatial Documentation of Geomorphological Changes and Geohazards in the Alpine Environment. *Land*, **13**, Article 112. https://doi.org/10.3390/land13010112

[21] Ahmad, N., Shafique, M., Hussain, M.L., Islam, F., Tariq, A. and Soufan, W. (2024) Characterization and Geomorphic Change Detection of Landslides Using UAV Multi-Temporal Imagery in the Himalayas, Pakistan. *Land*, **13**, Article 904. https://doi.org/10.3390/land13070904

[22] Wang, F., Wen, Z., Gao, Q., Yu, Q., Li, D. and Chen, L. (2024) Thermokarst Landslides Susceptibility Evaluation across the Permafrost Region of the Central Qinghai-Tibet Plateau: Integrating a Machine Learning Model with InSAR Technology. *Journal of Hydrology*, **642**, Article 131800. https://doi.org/10.1016/j.jhydrol.2024.131800

[23] Zhou, J.W., Jiang, N. and Li, H.B. (2024) Automatic Discontinuity Identification and Quantitative Monitoring of Unstable Blocks Using Terrestrial Laser Scanning in Large Landslide during Emergency Disposal. *Landslides*, **21**, 607-620. https://doi.org/10.1007/s10346-023-02169-6

[24] Li, Z.H., Jiang, N., Shi, A.C., Zhao, L.Y., Xian, Z., Luo, X.L. and Zhou, J.W. (2024) Reservoir Landslide Monitoring and Mechanism Analysis Based on UAV Photogrammetry and Sub-Pixel Offset Tracking: A Case Study of Wulipo Landslide. *Frontiers in Earth Science*, **11**, Article 133815. https://doi.org/10.3389/feart.2023.1333815

[25] Abdel-Maksoud, H. (2024) Combining UAV-LiDAR and UAV-Photogrammetry for Bridge Assessment and Infrastructure Monitoring. *Arabian Journal of Geosciences*, **17**, Article No. 144. https://doi.org/10.1007/s12517-024-11897-5

[26] Anand, A. and Bhardwaj, A. (2024) Unmanned Aerial Vehicles and Terrestrial Laser Scanning Are Used to Monitor Kshetrapal Landslides in the Chamoli Hazard Area of Upper Himalayan Region in Uttarakhand, India (No EGU24-11755). https://doi.org/10.5194/egusphere-egu24-11755

[27] Kaur, P. and Kumar, N. (2024) SIFTBCS: Scale Invariant Feature Transform Based Fuzzy Vault Scheme in Biometric Cryptosystem. *Multimedia Tools and Applications*, **83**, 28635-28656. https://doi.org/10.1007/s11042-023-16643-9

[28] Zhang, S.Y., Dong, J.X., Kabika, T.B., *et al.* (2024) LIE-DSM: Leveraging Single Remote Sensing Imagery to Enhance Digital Surface Model Resolution. *IEEE Transactions on Geoscience and Remote Sensing*, **62**, Article No. 5627512.

[29] Peternel, T., Urbančič, T., Trajkovski, K.K. and Grigillo, D. (2025) Landslide Volume and Runoff Monitoring Using UAV Photogrammetry. In: *Earth Observation Applications to Landslide Mapping, Monitoring and Modeling*, Elsevier, 173-198. https://doi.org/10.1016/b978-0-12-823868-4.00009-x

[30] Prakash, J., Greenaway, M.T. and Cools, K. (2024). Newton-Raphson Nonlinear Solver for Electric Field Integral Equation and Resistive Boundary Condition. 2024 *IEEE International Symposium on Antennas and Propagation and INC/USNC-URSI Radio Science Meeting* (*AP-S/INC-USNC-URSI*), Firenze, 14-19 July 2024, 483-484. https://doi.org/10.1109/ap-s/inc-usnc-ursi52054.2024.10686996